CHALMERS
UNIVERSITY OF TECHNOLOGY

Reduced-Order Modeling in Nonlinear Driveline Systems

System Identification of Periodic and Speed-Dependent Dynamics using Multi-Body Simulations

Degree project report in Systems, Control and Mechatronics

WILLIAM ENSTRÖM
ALEXANDER JOHNSSON

DEPARTMENT OF ELECTRICAL ENGINEERING
CHALMERS UNIVERSITY OF TECHNOLOGY
Gothenburg, Sweden 2026
www.chalmers.se

Degree project report 2026

Reduced-Order Modeling in Nonlinear Driveline Systems

System Identification of Periodic and Speed-Dependent Dynamics using Multi-Body Simulations

WILLIAM ENSTRÖM
ALEXANDER JOHNSSON

Department of Electrical Engineering
Chalmers University of Technology
Gothenburg, Sweden 2026

Reduced-Order Modeling in Nonlinear Driveline Systems
System Identification of Periodic and Speed-Dependent Dynamics using Multi-Body Simulations
WILLIAM ENSTRÖM, ALEXANDER JOHNSSON

Supervisors: Niclas Andersson, Per Sjövall and Ingemar Andersson, Volvo Cars
Examiner: Jonas Sjöberg, Department of Electrical Engineering

Degree project report 2026
Department of Electrical Engineering
Chalmers University of Technology
SE-412 96 Gothenburg
Sweden
Telephone +46 31 772 1000

Typeset in LaTeX
Gothenburg, Sweden 2026

Reduced-Order Modeling in Nonlinear Driveline Systems
System Identification of Periodic and Speed-Dependent Dynamics using Multi-Body Simulations
WILLIAM ENSTRÖM, ALEXANDER JOHNSSON
Department of Electrical Engineering
Chalmers University of Technology

Abstract

This thesis presents and investigates different approaches for constructing reduced-order BEV driveline models in state-space form using a data-driven approach. Existing Multi-Body Dynamic (MBD) models of the full driveline are often computationally demanding, while reduced models of sub-parts may lack a clear connection to the full-scale model and to one another. In order to improve simulation times while maintaining consistency with the more general MBD model, local Linear Time-Invariant (LTI) models are identified around selected operating points using subspace system identification methods and data generated from the larger MBD model. However, system internal periodic disturbances related to driveline rotation complicate the system identification as it contaminates the externally forced response. Two methods addressing this are investigated: Removing the frequency components associated with these disturbances from the data, or augmenting the model with additional input signals with those frequencies. Both methods improve the model quality by reducing the effect of the periodic disturbances. The model constructed by including additional input signals is also shown to more accurately reproduce the amplitude and frequency of the periodic disturbance. In order to model gyroscopic effects, such as resonance frequencies depending on the operating speed, several local LTI models are identified at different operating points. The local models are combined by either linear interpolation of the matrix elements, fitting a basis function to the matrix elements or by interpolating the outputs of each model. All three methods result in models with similar input-output accuracy, but differ in their requirements when creating the local models. In particular, methods based on output interpolation do not require system internal consistency between local models, unlike methods that rely on the local models sharing a common state-space realization. The disturbance-modeling approach based on additional input signals is also extended to the Linear Parametric Variant (LPV) framework, enabling the resulting models to capture both the speed-dependent system dynamics and the periodic disturbances associated with driveline rotation.

Keywords: System identification, reduced-order modeling, linear time-invariant systems, linear parameter-varying systems, multi-body dynamics, BEV driveline, periodic disturbances, gyroscopic effects, data-driven modeling

Preface

This report presents the result of our master's thesis project carried out at the Department of Electrical Engineering at Chalmers University of Technology during the spring of 2026 in cooperation with Volvo Car Corporation, Gothenburg, Sweden.

Acknowledgements

We would like to express our sincere gratitude to our supervisors, Niclas Andersson, Per Sjövall, Ingemar Andersson, and Jonas Sjöberg, for their invaluable guidance, patience, and support throughout the course of this research. Their insightful feedback and encouragement pushed us to sharpen our thinking, improve our technical work, and strengthen the writing of this thesis. We are also grateful to Jonas Sjöberg, in his role as examiner, for his careful review of this thesis and for the constructive comments and thoughtful questions that helped improve the final version of this work. We greatly appreciate the time and effort that they all devoted throughout the project.

William Enström, Alexander Johnsson, Gothenburg, August 2026

List of Acronyms

Below is the list of acronyms that have been used throughout this thesis listed in alphabetical order:

BEV	Battery Electric Vehicle
DOF	Degrees Of Freedom
LLS	Linear Least Squares
LPV	Linear Parametric Varying
LTI	Linear Time Invariant
MBD	Multi-Body Dynamic
MEP	Matrix Element Parameterization
N4SID	Numerical algorithms for Subspace State Space System IDentification
NRMSE	Normalized Root Mean Squared Error
PD	Periodic Disturbance
RPM	Revolutions Per Minute

Nomenclature

Below is the nomenclature of indices, parameters, and variables that have been used throughout this thesis.

Indices

i,j	Indices for matrix elements
k	Index for time steps
ℓ	Index for local working points
m	Index for basis functions
n	Index for frequencies

Parameters

Symbol	**Description**	**Unit**
ω	Angular frequency	[rad/s] or [Hz]
Ω	Shaft angular velocity (rotational speed)	[rad/s]
ρ	Scheduling parameter	–
T_s	Sampling period	[s]
θ_n	Rotation angle for disturbance n	[rad]
φ_n	Initial phase of disturbance n	[rad]
n_x	Number of states	–
n_u	Number of inputs	–
n_y	Number of outputs	–
N	Number of natural frequencies	–
N_ℓ	Number of local models / points	–
H	Number of disturbance frequencies	–
M	Number of basis functions	–

Variables

$\boldsymbol{M}$	Mass matrix
$\boldsymbol{V}$	Structural damping matrix
$\boldsymbol{K}$	Stiffness matrix
$\mathbf{F}$	External force vector
$\boldsymbol{q}$	Physical displacement vector
$\boldsymbol{x}$	State vector
$\boldsymbol{u}$	Input vector
$\boldsymbol{y}$	Output vector
$\boldsymbol{d}$	Disturbance vector
$\boldsymbol{A}, \boldsymbol{B}, \boldsymbol{C}, \boldsymbol{D}$	LTI state-space matrices
$\boldsymbol{G}$	Disturbance input matrix
$\boldsymbol{R}$	Rotational matrix (disturbance propagation)
$\mathcal{A}(\rho), \mathcal{B}(\rho), \mathcal{C}(\rho), \mathcal{D}(\rho)$	LPV (parameter-varying) state-space matrices
$\mathcal{H}(\rho)$	Augmented LPV model matrix
$\boldsymbol{H}_\ell$	Augmented local LTI model matrix
$\boldsymbol{T}_\ell$	Similarity transform matrix for local model ℓ
$\boldsymbol{\Theta}_m$	Coefficient matrix for basis function f_m
$\alpha_\ell(\rho)$	Scheduling-dependent weighting function for local model ℓ

General Notation Rules

- Vectors are denoted by boldface italic lowercase letters, e.g. $\boldsymbol{q}$, $\boldsymbol{x}$.
- Matrices are denoted by boldface italic uppercase letters, e.g. $\boldsymbol{M}$, $\boldsymbol{K}$.
- The external force vector is denoted $\mathbf{F}$, following common convention in structural dynamics, despite being a vector rather than a matrix.
- Scalars, including individual vector or matrix elements, are denoted by italic type, e.g. $q_{x,i}$, G_{11}.
- Calligraphic notation, e.g. $\mathcal{A}(\rho)$, is used exclusively to denote scheduling-parameter-varying (LPV) matrices, distinguishing them from the constant matrices of the corresponding LTI case.
- A dot above a variable denotes the total time derivative, e.g. $\dot{\boldsymbol{q}}$, $\ddot{\boldsymbol{q}}$.
- Subscripts denote indices (e.g. $\boldsymbol{q}_i$, $\boldsymbol{A}_\ell$), while a hat denotes an estimated quantity, e.g. $\hat{y}$.

Contents

List of Figures

List of Tables

1
Introduction

This chapter provides the background, describes the investigated problem and briefly mentions some related work. The goal of the project and its main contributions are stated.

1.1 Background

The design and dimensioning of mechanical driveline components in a Battery Electric Vehicle (BEV) require accurate estimations of quasi-static, transient and harmonic distributed loads that arise during dynamic operation. These loads act on and within the system and give rise to measurable structural responses such as forces, velocities and accelerations, here referred to as *responses*. Dynamic analysis of the structural system is critical for ensuring sufficient durability and performance, as well as low vibrations and disturbing noise. Existing simulation models of these systems are large-scale Multi-Body Dynamics (MBD) models, consisting of multiple flexible bodies connected through joints and force elements. Each body has several hundred Degrees Of Freedom (DOF) and is obtained by modal reduction of a detailed Finite Element Method (FEM) model, itself having DOF counts on the order of thousands to millions. The model assembly can be used to conduct virtual structure characterizing experiments by purposely applying different types of forces and torques and measuring system model responses.

While such large-scale MBD simulation models based on established physical principles can accurately describe BEV driveline systems, their high computational cost limits the efficiency in design analysis iterations, especially in the early stages when a large amount of simulations are needed for prediction of system performance of multiple solution candidates. It is therefore of interest to create reduced-order system models of the full MBD model that can provide computationally efficient and sufficiently accurate tools for driveline analyses. These reduced system models are beneficial, both by reducing simulation times when analyzing sub-parts of the larger model, and supporting the verification process of the MBD model.

Today, there exist simple ad-hoc model descriptions of both separate substructures and complete BEV drivelines that are conveniently used in various early-stage analyses. However, many such specific models are developed independently of each other or a more generally valid MBD model, which often results in inconsistencies between them. These inconsistencies limit the possibility of comparing results between reduced-order models and of using them to update and validate the common MBD model. Thus, there is a need for methods that generate locally valid reduced-order models while preserving a clear and consistent relationship to a common larger model.

An overview of the complete envisioned model reduction and validation workflow for the MBD model is illustrated in Figure 1.1. The process starts from the common MBD model, which is used to generate response datasets for multiple load levels and operating speeds. These response datasets are subsequently used for system identification to derive local reduced-order system models. The identified models can then be evaluated and compared across operating conditions and against physical measurements, providing a basis for updating and validating the reduced system representation and, ultimately, the common MBD model. This thesis focuses on the system identification stage of this workflow, where reduced-order models are derived from selected input-output response data.

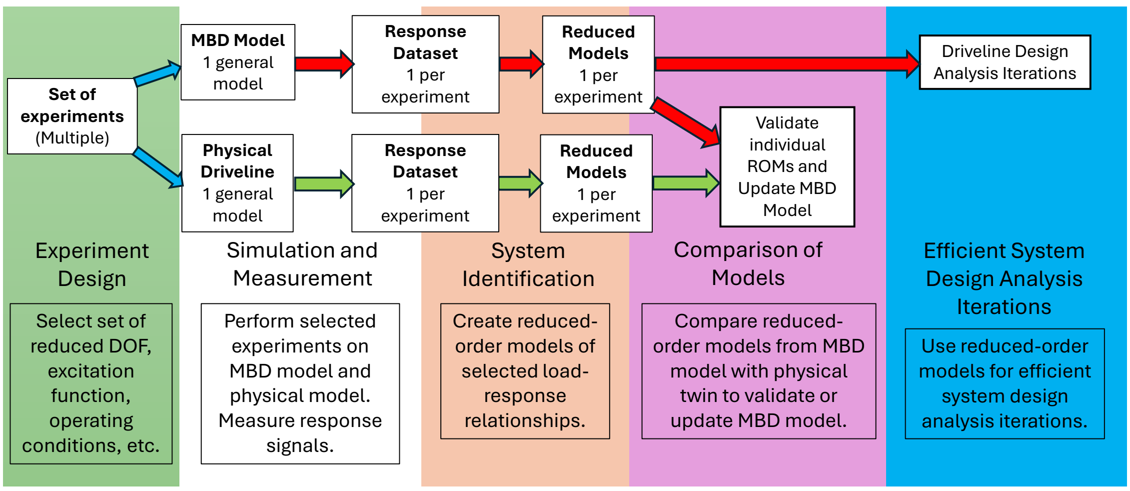

Figure 1.1: Workflow for model reduction and validation. A single MBD model and physical driveline form the common system-model representation. Multiple response datasets, covering different reduced-DOF sets, load levels, and operating speeds, are used to identify local reduced-order system models. These models support comparison with physical data and iterative updating and validation of the reduced system and common MBD model, enabling efficient system design analysis iterations.

1.2 Problem Description

To generate the data used for system identification, a large-scale MBD simulation model of the BEV driveline is used. A schematic representation of the MBD model with selected load and response signals is shown in Figure 1.2. The figure is simplified and does not show all joint models, housing structure and dynamometers. The model consists of three main shaft assemblies (each composed of several sub-shafts), a cast housing structure, and three dynamometers connected to the rotor shaft and the two output shafts. The parts are connected via individual nonlinear joint models such as bearings, spline couplings and gear meshes.

Among the available signals, the excitation torque $\tau_{\text{excitation}}$ applied to the input shaft and the translational bearing velocity v_x, are selected as input and output signals. Representing how torque variation from the motor affects vibration in a bearing connected to the input shaft rotating with rotational speed Ω. The objective is to identify reduced models that describe this input-output relationship.

The creation of the reduced models presents several challenges. Firstly, the rotational motion in combination with component stiffness asymmetries introduce periodic variations into the system response, which complicates the modeling and estimation process. Similarly, rotating masses cause gyroscopic effects which introduces varying system dynamics based on the operating speed. These two problems motivate the need for system identification approaches capable of capturing both periodic and speed-dependent dynamics, which are the central problems addressed in this thesis.

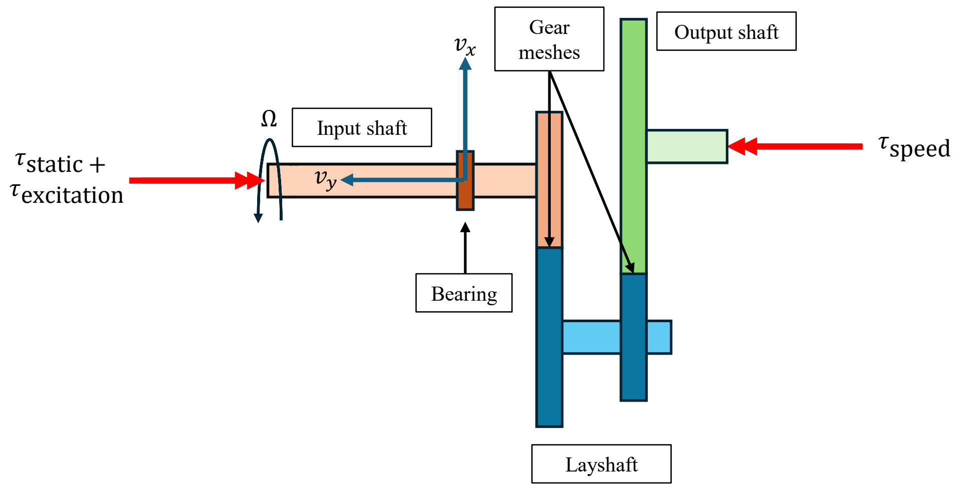

Figure 1.2: Schematic representation of the MBD model of the BEV driveline.

1.3 Related Work

Estimating LTI models of nonlinear systems by linearization around operating points is a well-established practice [1], and subspace methods such as Numerical algorithms for Subspace State Space System IDentification (N4SID) [2], are widely used to obtain a state-space representation directly from collected input-output data. Within the field of structural dynamics, subspace identification methods has been applied to many different areas such as modal analysis [3] and damage detection in structures [4], typically using data from physical measurements on real structures.

For systems with dynamics that vary with operating conditions, Linear Parametric-Varying (LPV) models provide a framework that extends LTI models by allowing the system matrices to depend on a measurable scheduling parameter [5]. LPV models have been applied to a wide range of systems such as a flexible wing aircraft [6] and DC motor systems with nonlinear dynamics [7]. One common approach to LPV modeling is to interpolate locally identified models to achieve a model that exhibits varying dynamics [8]. A key challenge in this approach is that the local models obtained must be expressed in the same state-space basis to achieve meaningful interpolation [9]. To obtain local models with a consistent basis methods such as SMILE [8] have been used.

A well-known challenge in the identification of rotating systems is the presence of disturbance that is periodic and driven by the rotating parts [10]. One common approach to this problem is to explicitly model the disturbances as external inputs [11]. In this context, this thesis applies these identification and modeling approaches to simulated data from a rotating driveline system.

1.4 Contributions

This thesis presents a data-driven approach for creating reduced-order models of a MBD model based on a BEV driveline. The main contributions are:

- Methods for deriving local LTI models using a subspace system identification method (Section 2.5).
- Methods for reducing influence of PDs present in the response from the MBD model (Section 3.3).
- Methods for modeling gyroscopic effects using an LPV-model, a comparison between different interpolation methods and ways to ensure smooth parameter variation (Section 3.4).

2

Foundations of Driveline Dynamics and System Modeling

This chapter mentions a few theoretical concepts relevant to the methods and models used in this thesis. The fundamentals of linear structural dynamics, vibrational modes, and multi-body driveline dynamics are briefly presented, followed by reduced-order modeling, state-space formulations, and system identification.

2.1 System Overview

Figure 2.1 depicts an overview of the MBD model of the BEV driveline used as the reference model, with a close-up view of the input shaft.

During simulation, the system is subjected to different forces $F(t)$, either applied externally, such as road-induced loads or motor torque fluctuations, or generated internally by the system during operation. The forces acting on the system cause it to deform or move over time, introducing motion in the form of vibration. The movement in a point i of the system can be described in generalized coordinates $\boldsymbol{q}_i = [q_{x,i}, q_{y,i}, q_{z,i}, q_{roll,i}, q_{pitch,i}, q_{yaw,i}]$, representing the translational and angular displacement in each coordinate. A vibrating system has a set of natural frequencies $[\omega_1 \ldots \omega_N]$, each associated with a corresponding deformation pattern that describes

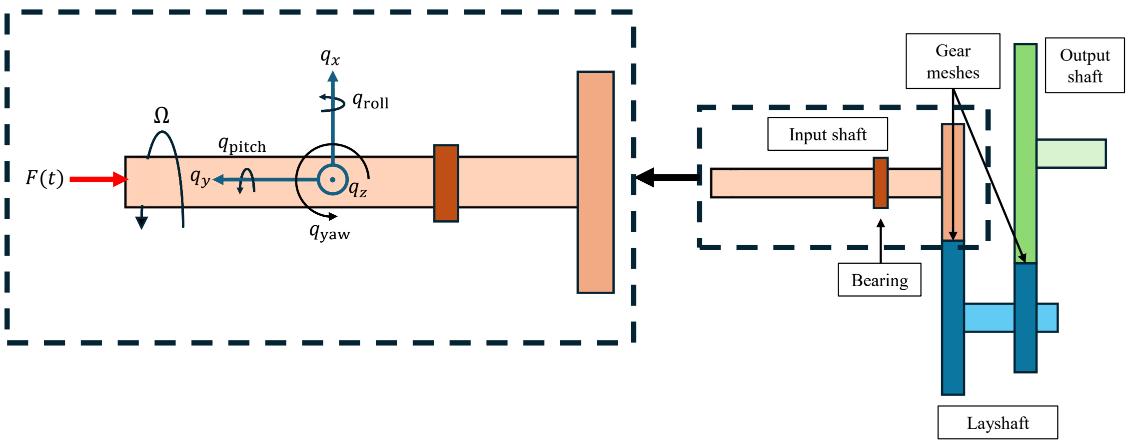

Figure 2.1: Schematic representation of MBD model of BEV driveline and close-up view of the input shaft.

the characteristic motion of the system when it is vibrating at that frequency. This deformation pattern is known as a mode shape and in combination with the corresponding natural frequency, it is commonly referred to as a vibrational mode. A mathematical description of this behavior is presented in Section 2.2.

As the structures in the BEV driveline are rotating, the vibrational response of the system depends on the rotational velocity. The shaft stiffness varies with rotational velocity, which affects the vibrational response of the system. In addition, the rotation introduces gyroscopic effects, which influence the dynamic characteristics of the system and can lead to changes in the natural frequencies of some modes, further explained in Section 2.3.1. The rotation also results in the shafts being subjected to dynamic forces with frequencies that depend on the rotational velocities of the individual shafts. For example, gear teeth interact a discrete number of times during each revolution, while centrifugal forces arise from mass imbalances in rotating shafts caused by material defects or deformations and asymmetrical stiffness varies while the contact point changes. Since these frequencies are directly related to the shaft rotational speeds, the frequencies of the resulting dynamic response also vary with the rotational speed. These effects are further explained in Section 2.3.2.

Also, in a BEV driveline, structural nonlinearities arise from several sources such as clearance between gear teeth, axial play in bearing seats and nonlinear material behavior such as nonlinear bearing stiffness [12]. These effects of the listed nonlinearities are further described in Section 2.3.3. To identify a linear representation of the system behavior these nonlinearities has to be suppressed during the identification. The methods of reducing them are described in Sections 3.1.1 and 3.2.2.

2.2 Structural Dynamics of Mechanical Systems

To describe the motion of a mechanical system, such as the BEV driveline in Figure 2.1, a commonly used structure dynamic model description is the linear second-order form of Newton's equation of motion,

$$\boldsymbol{M}\ddot{\boldsymbol{q}}(t) + \boldsymbol{V}\dot{\boldsymbol{q}}(t) + \boldsymbol{K}\boldsymbol{q}(t) = \mathbf{F}(t), \tag{2.1}$$

where t is absolute continuous time and a dot denotes the total time derivative, $\boldsymbol{M}$ is the mass matrix, $\boldsymbol{V}$ is the damping matrix, $\boldsymbol{K}$ is the stiffness matrix, $\mathbf{F}(t)$ is the external force vector and $\boldsymbol{q} = [\boldsymbol{q}_1, \ldots, \boldsymbol{q}_N]^\top$ is the physical displacement vector, describing the displacement in each DOF for all points of the system.

For rotating systems, such as the BEV driveline, the equation of motion can be written to show explicit speed dependencies as follows,

$$\boldsymbol{M}\ddot{\boldsymbol{q}}(t) + (\boldsymbol{V}_0 + \Omega\boldsymbol{G}_\mathrm{g})\dot{\boldsymbol{q}}(t) + (\boldsymbol{K}_0 + \Omega^2\boldsymbol{K}_\mathrm{c})\boldsymbol{q}(t) = \mathbf{F}(t) \tag{2.2}$$

where $\boldsymbol{V}_0$ and $\boldsymbol{K}_0$ are the non-rotating damping and stiffness matrices, $\boldsymbol{G}_\mathrm{g}$ is the gyroscopic matrix, $\boldsymbol{K}_\mathrm{c}$ is the centrifugal stiffness matrix, and Ω is the related scalar angular velocity [13].

2.2.1 Vibrations in Mechanical Systems

The solution to (2.1) consists of a homogeneous part $\boldsymbol{q}_{\mathrm{h}}(t)$, obtained by setting $\mathbf{F}(t) = 0$, and a particular part $\boldsymbol{q}_{\mathrm{p}}(t)$, giving the total response,

$$\boldsymbol{q}(t) = \boldsymbol{q}_{\mathrm{h}}(t) + \boldsymbol{q}_{\mathrm{p}}(t). \tag{2.3}$$

The homogeneous part represents the transient response due to initial conditions and will decay exponentially over time. The particular part represents the forced response caused by the excitation and will persist as long as the excitation is present [14]. This decomposition relies on the principle of superposition, which holds for linear systems and allows the total response to be expressed as the sum of individual contributions.

The n-th natural frequency ω_n of a system and the corresponding mode shape $\boldsymbol{\psi}_n$ can be obtained by solving the *undamped* eigenvalue problem,

$$(\boldsymbol{K} - \omega_n^2 \boldsymbol{M})\boldsymbol{\psi}_n = \mathbf{0}, \tag{2.4}$$

When the system is subjected to a periodic excitation with a frequency approaching ω_n, the response amplitude increases sharply. This phenomenon is known as *resonance*.

For lightly damped physical systems, such as the BEV driveline, the system eigenvalues become complex conjugate pairs,

$$\lambda_n = -\zeta_n \omega_n \pm \mathrm{i}\omega_{\mathrm{d},n}, \tag{2.5}$$

where ζ_n is the related ratio of critical damping and $\omega_{\mathrm{d},n} = \omega_n \sqrt{1 - \zeta_n^2}$ is the damped natural frequency [15]. The maximum response of a damped system therefore occurs at a frequency slightly below the undamped natural frequency.

2.2.2 Transformation to Modal coordinates

For large-dimensional system models, such as the BEV driveline with a large total number of DOFs, solving (2.1) often becomes computationally expensive. In such cases, it can be more efficient to transform the system into modal coordinates using the mode shapes obtained from (2.4), the physical coordinates are expressed as

$$\boldsymbol{q}(t) = \boldsymbol{\Psi}\boldsymbol{\eta}(t), \tag{2.6}$$

where $\boldsymbol{\Psi}$ is a matrix containing the mode shapes obtained from the eigenvalue problem,

$$\boldsymbol{\Psi} = \begin{bmatrix} \boldsymbol{\psi}_1 & \boldsymbol{\psi}_2 & \cdots & \boldsymbol{\psi}_N \end{bmatrix}, \tag{2.7}$$

and $\boldsymbol{\eta}(t)$ is the vector of modal coordinates. Transforming the system from physical to modal coordinates allows any solution of the system to be written exactly as a linear combination of all normal mode vectors [16].

The transformed system can then be reduced in dimension, by projecting the equations of motion onto a small modal subspace containing only a subset of the modes,

$$\boldsymbol{q}(t) \approx \boldsymbol{\Psi}_r \boldsymbol{\eta}_r(t), \tag{2.8}$$

where $\boldsymbol{\Psi}_r$ contains the dominant mode shapes and $\boldsymbol{\eta}_r(t)$ the corresponding modal coordinates. This usually works rather well in practice because, when the system is excited close to a resonance frequency, the response is often dominated by the corresponding mode vector. In cases where several vibrational modes are tightly spaced around the excitation frequency, several modes may contribute significantly to the response, but most other mode vectors contribute negligibly.

2.3 Multi-Body Driveline Dynamics

As mentioned in Section 2.1, the BEV driveline has multiple rotating shafts connected via nonlinear joint models causing gyroscopic effects, responses with frequencies related to the rotational speeds of the shafts and other structural nonlinearities. This section presents these effects in more detail.

2.3.1 Gyroscopic Effects

As the system rotates, gyroscopic effects arise that affects its characteristics. This can be seen in (2.2) where speed dependent terms $\boldsymbol{G}_\mathrm{g}$ and $\boldsymbol{K}_\mathrm{c}$ add to the static stiffness and damping matrices, resulting in change of individual natural mode frequencies and modes [13]. An example of this effect in the MBD model is shown in Figure 2.2, where the frequency response of the model changes based on operating speed.

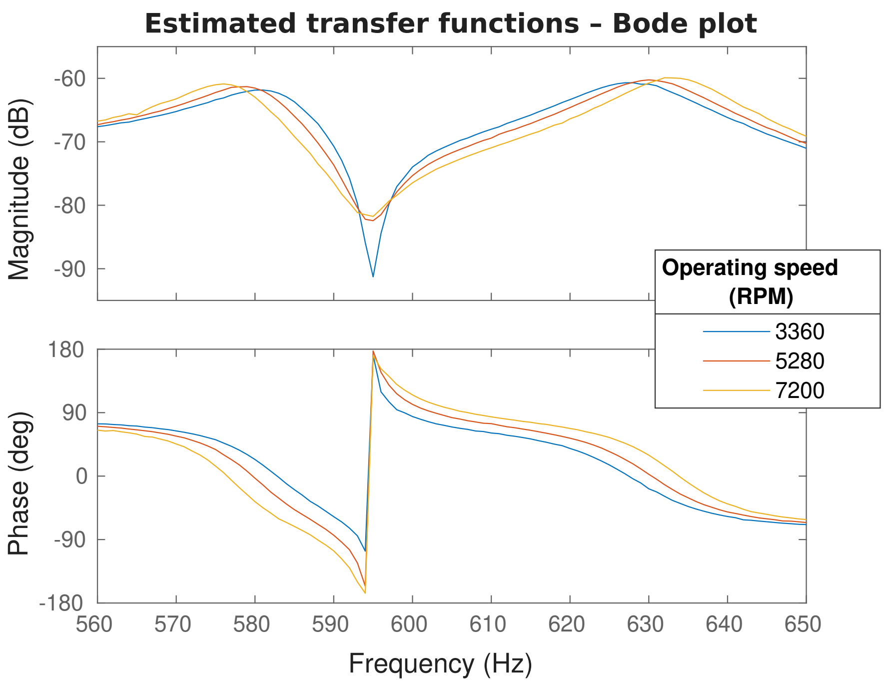

Figure 2.2: Bode plot (560-650 Hz) of estimated transfer functions of translational velocity in one of the bearings on the input shaft from Torque applied at input shaft at different operating speeds. Increasing the operating speed results in resonance frequencies moving further from each other.

2.3.2 Periodic Dynamics

When analyzing the response from an applied known excitation signal, it can be difficult to separate the corresponding forced response from other unknown periodic disturbances (PD) of the same frequency. Figure 2.3 shows the measured frequency response of translational velocity at the input shaft bearing, with and without external torque excitation. Two peaks in the response can be observed at 1x (136 Hz) and 2x (272 Hz) of the rotational frequency of the input shaft, both with and without external excitation. This indicates that the measured response from external excitation contains both the forced response and the response from unknown PDs. These PDs are plausibly caused by mass imbalances in the rotating shafts, either due to shaft misalignment or because of mass imbalances in the shafts themselves.

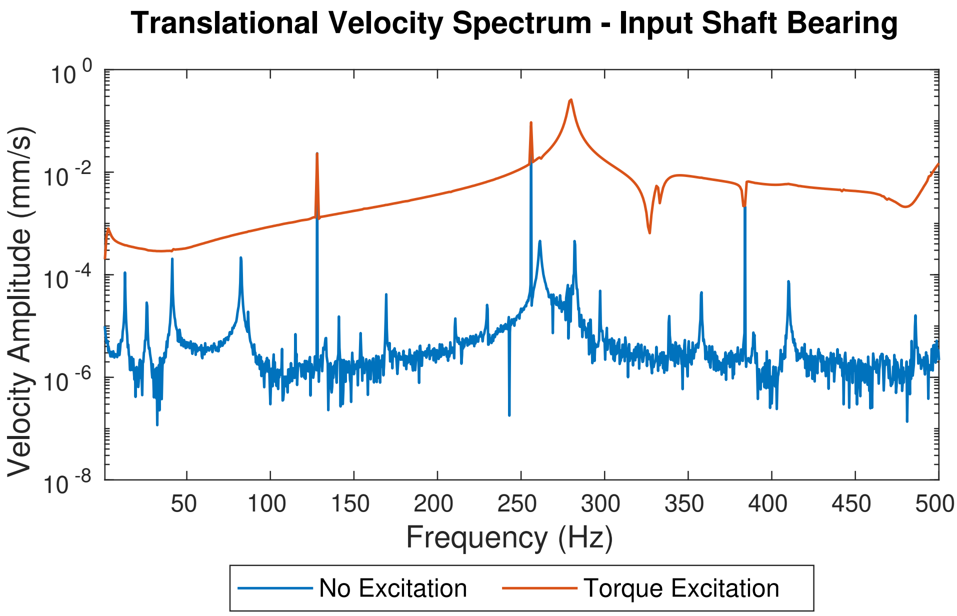

Figure 2.3: The measured response v_x when externally exciting the system (Figure 1.2) using $\tau_{\text{excitation}}$ with frequencies 0-1000 Hz using the multisine (in red), and the measured response v_x without any external excitation (in blue). The response peaks at frequencies at 136 Hz and 272 Hz are prevalent with or without external excitation.

Some of the periodic dynamics are also affected by the excitation signal. Figure 2.4 shows the frequency response when the system is externally excited by a single frequency independent of the shaft rotational speed. In addition to that externally driven frequency, the response energies also appear at frequencies that are even integer multiples of the shaft rotational speed. A plausible explanation for this behavior is existing asymmetries in shaft bending stiffness, resulting in a system internal pulsation twice for every full shaft revolution, which modulates the externally applied force to generate the observed side-bands. This calls for separating signal constraints when analyzing frequency responses from a multi-frequency excitation. For example, if the system is simultaneously excited by multiple fundamental and closely spaced frequencies, individual responses become difficult to identify, as each frequency bin contains responses from multiple sources.

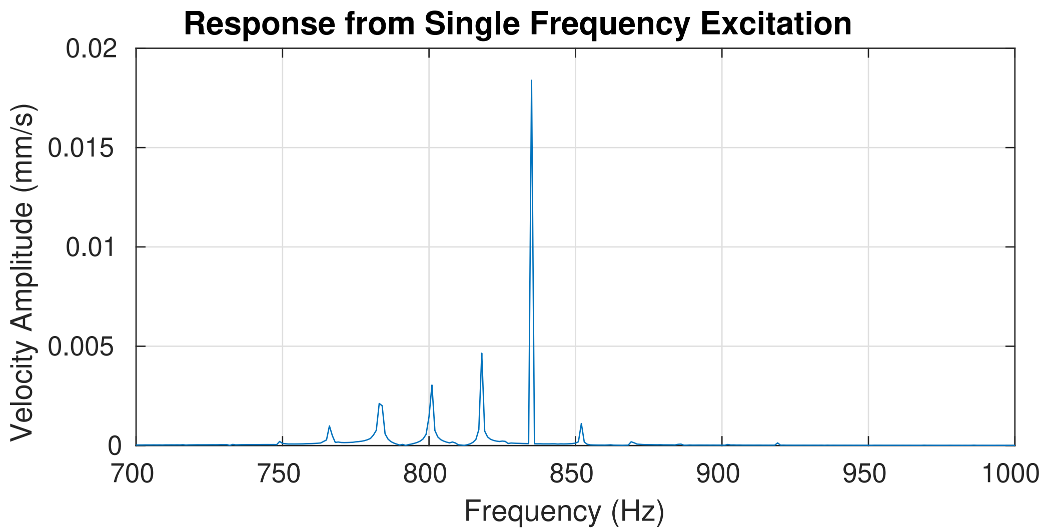

Figure 2.4: The frequency response from sinusoidal excitation of 835 Hz at 5000 RPM, measuring translational velocity in one of the bearings on the input shaft from Torque applied at the input shaft. The presence of sidebands around the excitation frequency indicates that the response is modulated by the rotational frequency of the input shaft.

2.3.3 Nonlinear Effects

As stated in Section 2.1, there are nonlinearities present in a BEV driveline. Clearance between gear teeth and axial play in bearing seats cause the driveline to behave nonlinearly whenever the torque changes sign. As torque crosses zero, for example during a transition from acceleration to braking, the components lose contact with each other, causing a discontinuity that a linear model cannot capture.

Nonlinear material behavior, such as nonlinear bearing stiffness, causes the driveline to respond differently at different load levels rather than follow a single linear relationship. As a result, for a large excitation amplitude, the local stiffness, and therefore the dynamic response, can differ near the positive and negative amplitude extremes of the excitation compared to lower load levels.

2.4 State-Space System Formulation

The second-order system in (2.1) and (2.2) can be rewritten in *state-space form* by introducing a state vector containing both displacements and velocities,

$$\boldsymbol{x}(t) = \begin{bmatrix} \boldsymbol{q}(t) \\ \dot{\boldsymbol{q}}(t) \end{bmatrix}, \tag{2.9}$$

so that the equations of motion are converted into an equivalent first-order representation. This state-space structure is a common linear model form used across multiple fields, and it models the system dynamics using first-order differential equations rather than a single higher-order equation. For integration into digital control and simulation, the continuous-time system is often discretized in time, resulting in,

$$\begin{aligned} \boldsymbol{x}_{k+1} &= \boldsymbol{A}\boldsymbol{x}_k + \boldsymbol{B}\boldsymbol{u}_k \\ \boldsymbol{y}_k &= \boldsymbol{C}\boldsymbol{x}_k + \boldsymbol{D}\boldsymbol{u}_k. \end{aligned} \tag{2.10}$$

where $\boldsymbol{x}_k$ denotes the system state, $\boldsymbol{u}_k$ the input and $\boldsymbol{y}_k$ the output vectors, respectively and the subscript k denotes the discrete time step. When the system matrices $\boldsymbol{A}, \boldsymbol{B}, \boldsymbol{C}$ and $\boldsymbol{D}$ are constant, the structure describes a Linear Time-Invariant (LTI) system.

The state-space structure introduces several benefits such as a matrix-based representation of systems with multiple inputs and outputs, and easier integration with control design and system analysis methods. Furthermore, local state-space models can serve as a basis for formulating a system as Linear Parametric-Varying (LPV) system in order to model system dynamics that vary with operating conditions.

In LPV systems the estimation takes parameter dependency into consideration, which results in the following form,

$$\begin{aligned} \boldsymbol{x}_{k+1} &= \mathcal{A}(\rho)\boldsymbol{x}_k + \mathcal{B}(\rho)\boldsymbol{u}_k \\ \boldsymbol{y}_k &= \mathcal{C}(\rho)\boldsymbol{x}_k + \mathcal{D}(\rho)\boldsymbol{u}_k. \end{aligned} \tag{2.11}$$

This can be viewed as a linear system in which the system matrices, instead of being constant, change depending on a measurable scheduling parameter ρ, allowing the model to capture changes in the system dynamics depending on the operating conditions [5]. Here, $\mathcal{A}(\rho)$, $\mathcal{B}(\rho)$, $\mathcal{C}(\rho)$, and $\mathcal{D}(\rho)$ denote the parameter-varying system matrices, distinguished by calligraphic notation from the constant matrices $\boldsymbol{A}$, $\boldsymbol{B}$, $\boldsymbol{C}$, and $\boldsymbol{D}$ of the LTI case in (2.10).

2.5 System Identification

The process of creating mathematical models of a dynamic system using measured data obtained from the system is called System Identification. A basic illustration of the concept is shown in Figure 2.5. The system is excited using predefined input signals, and the corresponding input-output data are collected. Model parameters are then estimated to reproduce the measured system behavior. Some limitations of system identification is that identified models are only valid under the same conditions used during the identification process (only same input signals, a certain operating point, etc.), and as models are constructed using only data, the model quality heavily depends on data quality. Measurement disturbances, wrong model structure and unknown inputs all risk negatively affecting the identified model [17].

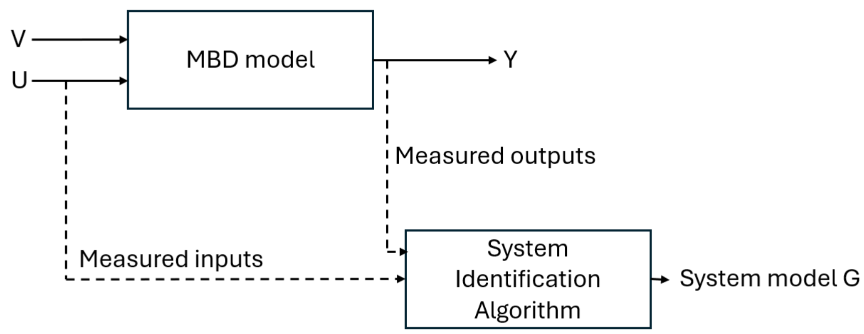

Figure 2.5: Basic concept of System identification. The inputs U are defined as measurable loads that drive the system, unlike the disturbances V that also drive the system but are unknown. The measured system response is defined as Y.

The system identification algorithm used in this work is Numerical algorithms for Subspace State Space System Identification (N4SID) with Prediction Error Minimization (PEM), which generates a system model on state-space form. N4SID is a subspace-based identification method that estimates state-space models directly from input–output data [2]. Because there exist multiple realizations that can represent the same input-output behavior, the resulting state-space realization is not unique, and the state vector does not necessarily correspond to physical coordinates.

The method relies on linear algebra techniques such as singular value decomposition and is well suited for multivariable systems and relatively large data sets. An additional advantage of N4SID is that the algorithm does not require any initial guess of the system parameters [2]. After the initial model is obtained from N4SID, it is refined using the optimization algorithm PEM. PEM formulates system identification as an optimization problem where the model parameters are adjusted to minimize the prediction error between the measured outputs and the model predictions. This combination of N4SID and PEM provides a robust identification procedure: N4SID supplies a reliable initial state-space realization, and PEM is used to further optimize the model parameters with respect to the measured data.

3

Methodological Approach

This chapter presents the methods used throughout this thesis, following the pipeline introduced in Section 3.1 (Figure 3.1). Section 3.1 motivates the overall approach, Section 3.2.1 describes the experimental setup, and Sections 3.3 and 3.4 describe the methods used for handling periodic disturbances and gyroscopic effects, respectively.

3.1 Reduced Modeling Approach

This section presents and motivates the selected approach for creating reduced models. As stated in Section 1.1, there is a need for methods that create reduced models with a common connection to the larger model. This motivates the use of data-driven modeling, with simulation data gathered from the existing MBD model.

An overview of the method is depicted in Figure 3.1. Each block is explained in further detail in the sections below. The pipeline consists of the following steps. Block A is the full-order MBD model of the BEV driveline (Figure 1.2), used to generate simulation data. Block B is a set of experiments performed at selected fixed operating points, producing excitation-response data (Sections 3.1.1 & 3.2). Block C are two approaches for handling PDs mentioned in Section 2.3.2 in the response: removing the affected frequency components or modeling them explicitly

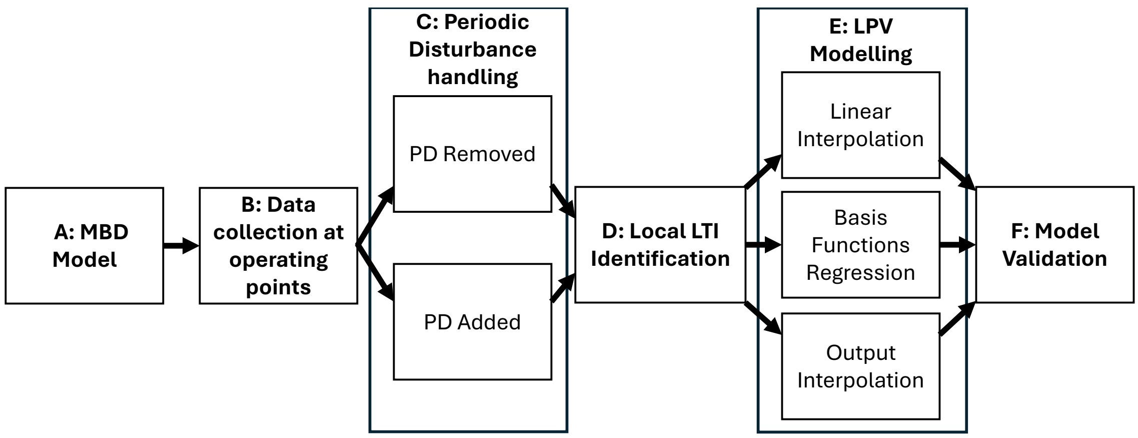

Figure 3.1: Overview of the reduced-order modeling pipeline used in this thesis. Each labeled block is described in Section 3.1 and referred to throughout the following chapters.

as additional inputs, described in Section 3.3.

Block D is the identification of local LTI models from this data using subspace identification (Section 3.1.2). Block E combines local LTI models identified at multiple operating points into a single LPV model capturing speed-dependent dynamics (Section 3.4). Block F is the validation of the resulting models against independent MBD simulation data (Section 3.5).

3.1.1 Operating-Point-Dependent Modeling

This section addresses the operating points in block B in Figure 3.1. To enable the use of linear system analysis and identification methods, the system is linearized around selected operating points. The MBD model is simulated at a set of predefined fixed rotational speed and braking load amplitudes. To reduce the effects of clearance between gear teeth and axial play in bearing seats discussed in Section 2.3.3, the constant braking load was selected to be large enough that the combined load from excitation and braking torque (Figure 3.2) keep the same sign throughout the experiments.

The exact choice of the operating points depends on the specific experiment and are presented in detail in their respective sections.

3.1.2 System Identification Approach

This section addresses block D in Figure 3.1. Linear state-space models are identified using `ssest()` from the MATLAB System Identification toolbox [18]. This method is based on the N4SID algorithm combined with the PEM, further explained in Section 2.5, and estimates models on the state-space form in (2.10).

Using system identification with the selected excitation and response signals mentioned in Section 3.2.1, state-space models obtained for each operating condition. The models describe the input-output relationship for the chosen signals and operating conditions and can be used to simulate a response from an input signal much faster than the existing MBD model.

3.2 Experimental Setup

This section addresses blocks A and B in Figure 3.1. The existing MBD model presented in Figure 1.2 is used as the reference large-scale model throughout this thesis. The model is implemented in the simulation program Excite M [19]. This model serves as the baseline from which reduced-order models are derived and evaluated from. This section presents the simulation setup and excitation signals used in combination with the MBD model to generate response data that are then used for system identification.

3.2.1 Simulation Setup and Data Collection

The response from the MBD model is simulated using co-simulation between Excite and MATLAB/Simulink [20], with the torque and speed at the dynamometers being controlled outside of Excite via a measurement and control system implemented in MATLAB/Simulink and the dynamics simulated in Excite. The simulations are carried out in the time domain, where inputs and outputs are measured and evaluated at every time step. Measurements are carried out after the transient response, explained in Section 2.2.1, has decayed and the system has reached steady-state operation at the selected operating point. An overview of the simulation setup can be seen in Figure 3.2. The signals applied to the system consists of three components: a static braking torque, a speed controlling torque and an excitation signal.

The static braking torque is applied to the input shaft and defines the load amplitude operating point at which the simulation is performed. Another purpose of the static torque is to keep the system preloaded to reduce nonlinear effects associated with low loads in gear contacts, as described in Section 2.3.3.

The speed controlling torque is applied at the output shaft and controls the rotational speed of the system. The torque is computed with a PID controller implemented in MATLAB.

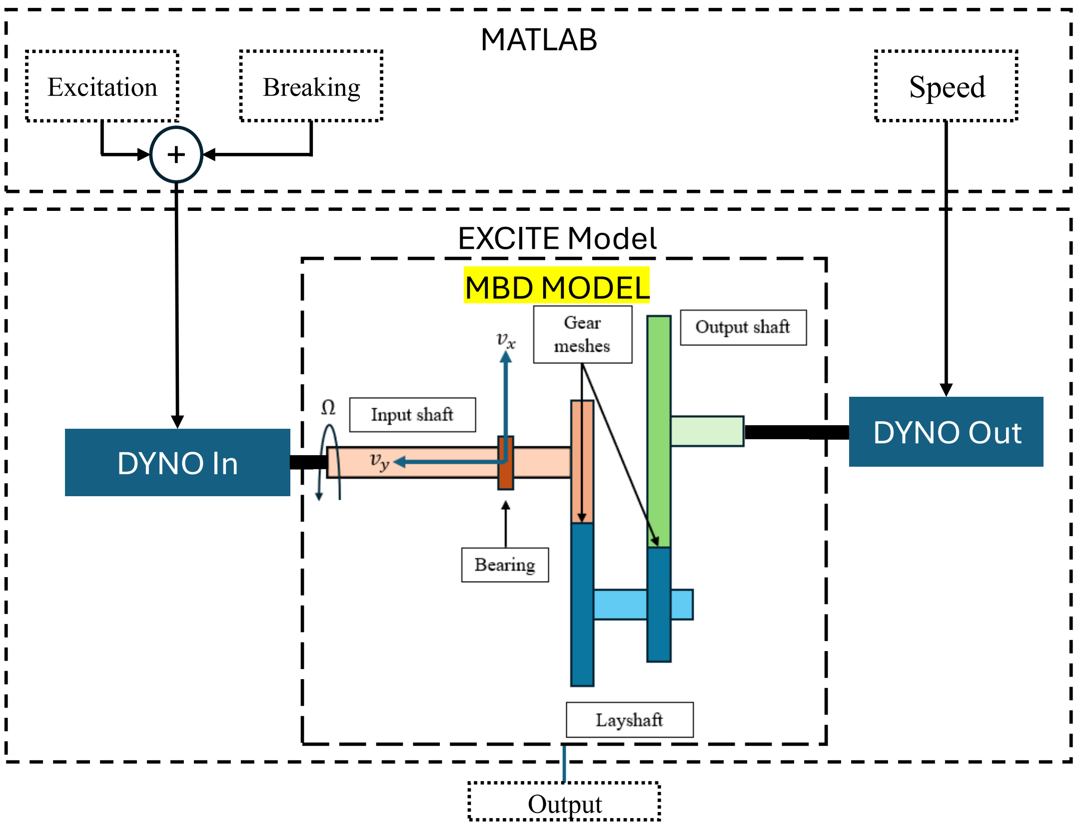

Figure 3.2: Experiment setup with co-simulation between Excite and MATLAB.

The excitation signal is an additional torque signal applied to the system together with the static torque at the input shaft. The design of the excitation signal is further explained in Section 3.2.2. This signal is used together with the response signal in the system identification algorithm.

The output signal used in the system identification algorithm is the simulated response of the translational velocity at a bearing on the input shaft.

3.2.2 Excitation Signal Design

The proposed excitation signal type is a multisine signal. The set of excitation frequencies are selected using

$$u(t) = \sum_{n=1}^{N} A_n \cos(2\pi f_n t + \phi_n), \tag{3.1}$$

where A_n and ϕ_n are the input amplitude and phase shift at frequency f_n. Exciting the system with multiple frequencies at once reduces simulation time compared to stepping one frequency at a time.

In order to reduce the load-dependent nonlinear material behavior of the driveline, discussed in Section 2.3.3, the total signal amplitude must be kept below a certain level. However, limiting the total signal amplitude also constrains the amplitude that can be used at each individual frequency, which in turn reduces the signal-to-noise ratio. To address this, Schroeder phasing is used, where the phase for each signal is determined by

$$\phi_n = \frac{-n(n-1)\pi}{N_f}, \tag{3.2}$$

where ϕ_n is the phase shift at frequency n, and N_f is the number of frequencies used to determine the phase shifts [21]. This minimizes the peak amplitude of the combined multisine signal for a given amplitude per frequency, thereby allowing a higher amplitude to be used at each frequency without exceeding the maximum total signal amplitude.

When gathering data in the frequency domain it is possible to combine data from separate runs, allowing for strategic frequency choices decreasing the risk of the frequency response being caused by sources other than the excitation at the same frequency, instead of also including response from sidebands. The frequencies for each run are selected so that the most prominent sidebands described in Section 2.3.2 do not end up at the same frequency bin as an excited frequency.

3.3 Identification Under Periodic Disturbances

This section addresses block C in Figure 3.1. As stated in Section 2.3.2, mass imbalances in the system caused by, for example, shafts being skewed by applied torque, asymmetrical shafts or similar, causes periodic responses from the system that are not caused by the excitation signal, as can be seen in Figure 2.3. These periodic responses complicate the identification process as the forces causing them are not measurable. The system identification algorithm tries to model these periodic responses as a response from the excitation, resulting in the disturbance being modeled as undamped or very lightly damped oscillations, making the identified system unstable or inaccurate.

With the presence of these PDs there exists different approaches on how to handle them. One approach is to only consider and model the input-output relationship of the system. Another approach is to attempt to model the true response of the system including disturbances as even though phase is unknown and not measured, amplitude and frequency are directly related to a known rotational speed. The application of these two approaches are presented in the two following sections.

3.3.1 Removing Disturbance Frequencies

If the goal is to model the input-output behavior and ignore the disturbance response, then the frequency bins of the PDs can be removed from the frequency data used during the identification process.

Removing data points containing peaks from PDs reduces the risk of those peaks being modeled as resonances. Although, if they are close to true resonance peaks, removing data points might cause the identification algorithm to model the peak slightly wrong when reducing frequency resolution.

3.3.2 Including Disturbances in Model

If the goal is to enable simulation with the inclusion of disturbance response, the disturbances must be included in the model. In order to keep the disturbance response separate from the system dynamics, the following model structure [11] is used:

$$\begin{aligned} \boldsymbol{x}_{k+1} &= \boldsymbol{A}\boldsymbol{x}_k + \boldsymbol{B}\boldsymbol{u}_k + \boldsymbol{G}\boldsymbol{d}_k \\ \boldsymbol{y}_k &= \boldsymbol{C}\boldsymbol{x}_k + \boldsymbol{D}\boldsymbol{u}_k. \end{aligned} \tag{3.3}$$

The difference from the regular state-space model (2.10) is the inclusion of the term $\boldsymbol{G}\boldsymbol{d}_k$. This term separates the disturbances from the system dynamics and treats them as unknown inputs. It consists of the disturbance vector $\boldsymbol{d}_k$ and the matrix $\boldsymbol{G}$ which relates the disturbances to the state vector.

3.3.2.1 Identification step

When considering the specific case of the disturbances observed in the response of the MBD model, see Figure 2.3, the amplitude and phase of the loads causing the PDs are not explicitly known. However, their frequency content is clearly seen to align with integer multiples of the rotational frequencies of the three shafts. Using this information the disturbance vector was defined as,

$$\boldsymbol{d} = \begin{bmatrix} \cos(\omega_{\mathrm{d},1}) \\ \sin(\omega_{\mathrm{d},1}) \\ \vdots \\ \cos(\omega_{\mathrm{d},H}) \\ \sin(\omega_{\mathrm{d},H}) \end{bmatrix} \tag{3.4}$$

where $\omega_{\mathrm{d},1}, \dots, \omega_{\mathrm{d},H}$ are the observed disturbance frequencies. Using this model structure, the goal is to use the system identification algorithm to also estimate the matrix $\boldsymbol{G}$. As the N4SID algorithm estimates a model structure on the regular state-space form (2.10), this was done by supplying the $\boldsymbol{d}_k$ as additional inputs to the system identification algorithm to estimate,

$$\begin{aligned} \boldsymbol{x}_{k+1} &= \boldsymbol{A}\boldsymbol{x}_k + \begin{bmatrix} \boldsymbol{B} & \boldsymbol{G} \end{bmatrix} \begin{bmatrix} \boldsymbol{u}_k \\ \boldsymbol{d}_k \end{bmatrix} \\ \boldsymbol{y}_k &= \boldsymbol{C}\boldsymbol{x}_k + \boldsymbol{D}\boldsymbol{u}_k. \end{aligned} \tag{3.5}$$

The reason behind assigning both a cosine and a sine signal with each observed disturbance frequency is to enable the elements in $\boldsymbol{G}$ to represent each disturbance frequency with arbitrary amplitude and phase shift, allowing the response at that frequency to differ in both amplitude and phase from the corresponding input.

$$G_{11}\cos(\omega_1) + G_{12}\sin(\omega_1) = a_1\cos(\omega_1 - \phi_1), \tag{3.6}$$

where

$$a_1 = \sqrt{G_{11}^2 + G_{12}^2}, \quad \phi_1 = \arctan\left(\frac{G_{12}}{G_{11}}\right). \tag{3.7}$$

3.3.2.2 Disturbances as States

Once the model including disturbances (3.5) has been estimated, the simulation of the system response with the disturbances can be simulated. In the initial estimated model structure, the model requires $2 \cdot N_{dist}$ additional input signals, the same ones used in (3.4). Additionally, if the rotational speed of the system varies, the disturbance input signals must be adjusted so that the sinusoidal frequencies remain aligned with the rotational speed.

To address these challenges and simplify the simulation step, the model structure in (3.5) can be modified by moving the disturbances into the state vector as additional states, as was done in [22], resulting in the following augmented model structure,

$$\begin{aligned} \begin{bmatrix} \boldsymbol{x}_{k+1} \\ \boldsymbol{d}_{k+1} \end{bmatrix} &= \begin{bmatrix} \boldsymbol{A} & \boldsymbol{G} \\ \boldsymbol{0} & \boldsymbol{R} \end{bmatrix} \begin{bmatrix} \boldsymbol{x}_k \\ \boldsymbol{d}_k \end{bmatrix} + \begin{bmatrix} \boldsymbol{B} \\ \boldsymbol{0} \end{bmatrix} \boldsymbol{u}_k \\ \boldsymbol{y}_k &= \begin{bmatrix} \boldsymbol{C} & \boldsymbol{0} \end{bmatrix} \begin{bmatrix} \boldsymbol{x}_k \\ \boldsymbol{d}_k \end{bmatrix} + \boldsymbol{D}\boldsymbol{u}_k \end{aligned} \tag{3.8}$$

Here $\boldsymbol{R}$ is a rotational matrix,

$$\boldsymbol{R}_n = \begin{bmatrix} \cos(\theta_n) & -\sin(\theta_n) \\ \sin(\theta_n) & \cos(\theta_n) \end{bmatrix} \tag{3.9}$$

where $\theta_n = \omega_{\mathrm{d},n} T_s$, where T_s is the sampling period, resulting in the disturbance states evolving as sinusoidal signals with frequency $\omega_{\mathrm{d},n}$, which is related to the rotating speed of the system. By performing this modification into the model structure in (3.8), the simulation is simplified by allowing the disturbance-causing load signals to be generated internally by updating the matrix $\boldsymbol{R}$ according to the rotational speed and specifying the initial disturbance states as,

$$\boldsymbol{d}_0 = \begin{bmatrix} \cos(\varphi_1) \\ \sin(\varphi_1) \\ \vdots \\ \cos(\varphi_{\mathrm{H}}) \\ \sin(\varphi_{\mathrm{H}}) \end{bmatrix}, \tag{3.10}$$

where φ_n denotes the initial phase of the n-th disturbance. The signal is then propagated by the rotational matrix.

3.4 LPV Modeling Approaches

This section addresses block E in Figure 3.1. In order to model the speed-dependent dynamics of the system, additional modeling strategies are required. As mentioned in Section 3.1.1 the system is linearized around fixed rotating speed and load amplitude. As mentioned in Section 1.4, this work presents methods for modeling the gyroscopic effects, which are dependent on rotating speed, but the methods should also be applicable to changes in load amplitudes.

To model the gyroscopic effects, an LPV system model structure (2.11) is selected, with the scheduling parameter ρ being the rotational speed of the input shaft. The idea is to use local linear models that are identified at different operating points of different rotational speeds to identify the parameter dependency. There are multiple ways to parameterize the local LTI models to create an LPV model. Three methods were investigated, Two methods focus on creating a parameterization of the matrix elements of the LPV model, while the final method focuses on interpolating the outputs of the local model. The methods are presented in Sections 3.4.1 and 3.4.2. The methods are presented for the case when ρ is a single parameter, but the same approach could be used for multiple scheduling parameters.

3.4.1 Matrix Element Parametrization

This section presents the two methods of Matrix Element Parameterization (MEP) to create an LPV model. Both methods require the local models to be *coherent*. This means that all local models must share the same state basis and must contain the same modes. If the local models are not coherent, the interpolation between the local models is not trivial [9]. Two methods for solving this problem is presented in the next section.

Before considering the specific parameterization methods, it is useful to distinguish between parameterizations that pass exactly through the identified data points and those that provide a smooth approximation of the data. An example illustrating this difference between the two MEP methods described in Sections 3.4.1.2 and 3.4.1.3 is shown in Figure 3.3. The figure shows two $\boldsymbol{A}$-matrix elements from locally identified LTI state-space models at rotating speeds between 2880–6780 RPM.

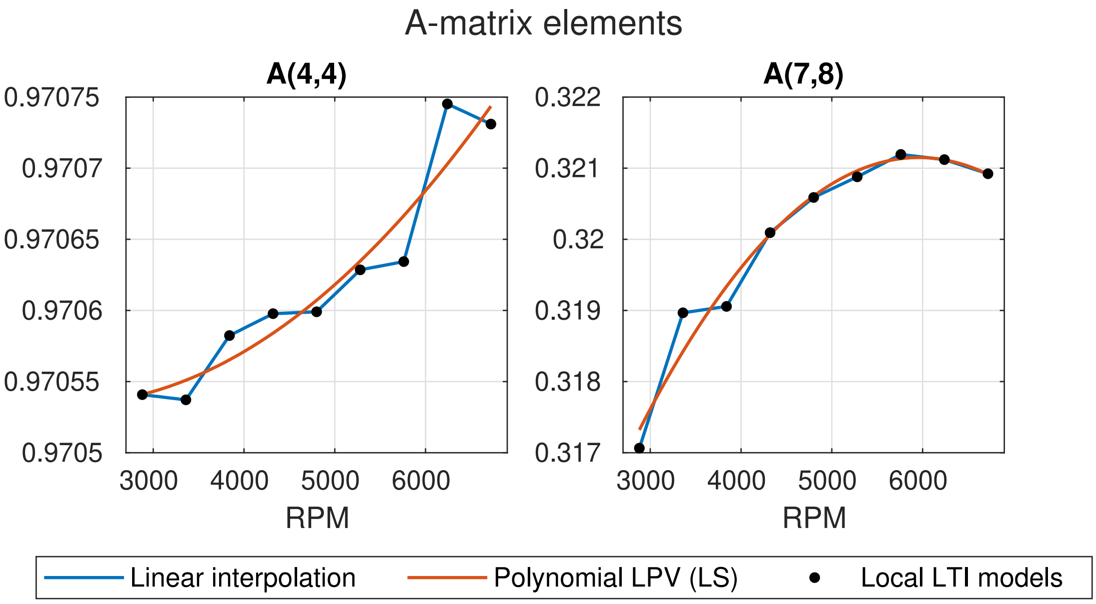

Figure 3.3: Different methods of parameterization of matrix element values.

In the figure, the linear interpolation passes exactly through all local LTI models, but results in a non-smooth curve. In contrast, the polynomial parameterization uses linear least-squares (LLS) regression to obtain a smooth curve, at the cost of not passing exactly through the local models at the operating points where they were identified. To determine which MEP methods that are preferable when modeling the BEV driveline, the performance of the different parameterizations are compared in Chapter 5.

3.4.1.1 Achieving Coherent Models

As mentioned in the first paragraph of the previous section, the local models must be coherent to allow for interpolation between them. Two methods for improving model coherence are presented below. The first approach is summarized as follows:

1. An initial local model is identified at a given operating point (rotational speed) using system identification. Models are expressed in a canonical state-space form with a block-diagonal structure to reduce the amount of parameters.
2. The identified model is then used as an initial guess for the identification of the new local model at a neighboring operating point. With the idea that it should increase the chance of coherent models.
3. This procedure is then repeated iteratively throughout the operating range, where each newly identified model served as the initial guess for the subsequent

estimation.

The second investigated method, known as the SMILE method [8] is presented below:

Compute the observability matrix of all local LTI models $1, \ldots, N_\ell$. Using the first model as a reference. Define the similarity transformation as a multiplication between Moore-Penrose pseudo inverse of observability matrix from the first model, and the observability matrix of LTI model ℓ:

$$\boldsymbol{T}_\ell = \boldsymbol{O}_1^\dagger \boldsymbol{O}_\ell \tag{3.11}$$

Transform each state-space matrix at ℓ:

$$\boldsymbol{A}_{\mathrm{coh},\ell} = \boldsymbol{T}_\ell \boldsymbol{A}_\ell \boldsymbol{T}_\ell^{-1}, \quad \boldsymbol{B}_{\mathrm{coh},\ell} = \boldsymbol{T}_\ell \boldsymbol{B}_\ell, \quad \boldsymbol{C}_{\mathrm{coh},\ell} = \boldsymbol{C}_\ell \boldsymbol{T}_\ell^{-1}, \tag{3.12}$$

For the SMILE method to produce coherent models it requires fully observable and controllable LTI models that have identified the same modes.

3.4.1.2 Linear Interpolation

Once coherent local models have been obtained, a linear interpolation between the models can be done. At a given value of the scheduling parameter ρ, each element of the state-space matrices is obtained by linear interpolation between the two nearest LTI models defined at ρ_1 and ρ_2, where $\rho_1 \leq \rho \leq \rho_2$.

$$\mathcal{A}_{i,j}(\rho) = \frac{\rho_2 - \rho}{\rho_2 - \rho_1} A_{i,j}^{(1)} + \frac{\rho - \rho_1}{\rho_2 - \rho_1} A_{i,j}^{(2)} \tag{3.13}$$

Where $\mathcal{A}$ is the LPV model matrix and $\boldsymbol{A}^{(1)}$ and $\boldsymbol{A}^{(2)}$ are the locally estimated LTI model A-matrices. The interpolation is done individually for all matrix elements. The interpolation was done using the MATLAB function `ssInterpolant(ssArray)` where `ssArray` is an array of the LTI models. The values of ρ was set using the field names of `ssArray.SamplingGrid`.

3.4.1.3 Basis Functions Regression

Instead of interpolating only between the two models estimated at scheduling parameter values closest to the current parameter value, a fit can be performed using all available models. A method of this was presented in [8] which consist of selecting a set of basis functions a-priori, and fitting the coefficients to the set of locally estimated LTI models. Assuming the existence of locally estimated coherent LTI models, each can be written as an augmented matrix

$$\boldsymbol{H}_\ell = \begin{bmatrix} \boldsymbol{A}_\ell & \boldsymbol{B}_\ell \\ \boldsymbol{C}_\ell & \boldsymbol{D}_\ell \end{bmatrix} \in \begin{bmatrix} \mathbb{R}^{n_x \times n_x} & \mathbb{R}^{n_x \times n_u} \\ \mathbb{R}^{n_y \times n_x} & \mathbb{R}^{n_y \times n_u} \end{bmatrix} \tag{3.14}$$

for local LTI models $\ell = 1, \ldots, N_\ell$, the corresponding global LPV model is then defined as

$$\mathcal{H}(\rho) = \begin{bmatrix} \mathcal{A}(\rho) & \mathcal{B}(\rho) \\ \mathcal{C}(\rho) & \mathcal{D}(\rho) \end{bmatrix}. \tag{3.15}$$

The method can then be summarized as follows,

1. Choose a set of basis functions $f_m(\rho) : \mathbb{R}^d \to \mathbb{R}$, for $m = 1, \ldots, M$.
2. Parameterize the global LPV model as a basis-function expansion

$$\mathcal{H}(\rho) = \sum_{m=1}^{M} f_m(\rho)\, \mathbf{\Theta}_m, \tag{3.16}$$

   where $\mathbf{\Theta}_m \in \mathbb{R}^{(n_x+n_y)\times(n_x+n_u)}$ are unknown coefficient matrices for each basis function.
3. Determine the coefficient matrices $\mathbf{\Theta}_m$ such that the LPV model approximates the locally identified models over the scheduling-parameter samples. Specifically, given scheduling-parameter samples $\{\rho_\ell\}_{\ell=1}^{N_\ell}$ and corresponding local models $\boldsymbol{H}_\ell$, the coefficients are obtained by solving

$$\min_{\{\mathbf{\Theta}_m\}} \sum_{\ell=1}^{N_\ell} \left\| \boldsymbol{H}_\ell - \sum_{m=1}^{M} f_m(\rho_\ell)\, \mathbf{\Theta}_m \right\|_F^2, \tag{3.17}$$

   where $\|\cdot\|_F$ denotes the Frobenius norm. Since the basis functions are fixed, the problem is linear in the unknown matrices $\mathbf{\Theta}_m$ and reduces to a LLS problem [8].

Using this method a single function for each element can be achieved giving smoothly varying matrix elements. The basis functions considered were,

$$f_1(\rho) = 1, \quad f_2(\rho) = \rho, \quad f_3(\rho) = \rho^2. \tag{3.18}$$

The selection of these basis functions is motivated by the structure of the equation in Section 2.3.1, where gyroscopic effects show linear dependence and centrifugal stiffening show quadratic dependence on the rotational speed. While the identified model is purely data-driven and does not rely on physical coordinates, this observation provides some intuition for selecting a low-order polynomial representation of the parameter dependence.

Two LPV models were then estimated using different subsets of these basis functions:

$$\mathcal{H}_1(\rho) = \mathbf{\Theta}_1 + \rho\mathbf{\Theta}_2, \tag{3.19}$$
$$\mathcal{H}_2(\rho) = \mathbf{\Theta}_1 + \rho\mathbf{\Theta}_2 + \rho^2\mathbf{\Theta}_3. \tag{3.20}$$

3.4.2 Output Interpolation

As previously mentioned in Section 3.3 both MEP methods mentioned the previous section requires that the local LTI models are coherent. As this can sometimes be difficult to achieve, an alternative method is presented here which does not require that the local models are coherent. This relaxation comes at the cost of losing a compact and physically interpretable state-space representation. Instead, the primary objective of this method is to achieve accurate input–output behavior across the scheduling-parameter domain.

The basic idea of the method is to construct a large state-space model by combining all local LTI models. Each local model contributes its own state vector, and the global state vector is formed by concatenating these states [23]. For a collection of local models the combined dynamics are given by

$$\boldsymbol{x}_\ell(k+1) = \boldsymbol{A}_\ell \boldsymbol{x}_\ell(k) + \boldsymbol{B}_\ell \boldsymbol{u}(k), \tag{3.21a}$$

$$\boldsymbol{y}(k) = \sum_{\ell=1}^{N_\ell} \alpha_\ell(\rho)\Big(\boldsymbol{C}_\ell \boldsymbol{x}_\ell(k) + \boldsymbol{D}_\ell \boldsymbol{u}(k)\Big) \tag{3.21b}$$

where $\alpha_\ell(\rho)$ are a set of scheduling-dependent weighting functions associated with the ℓ-th local model, $\alpha_\ell : \mathbb{S} \to [0,1]$ where $\mathbb{S}$ is the interval in which the local models are to be interpolated. The weighting functions are typically bell shaped and must satisfy,

$$\sum_{\ell=1}^{N_\ell} \alpha_\ell(\rho) = 1 \quad \text{for all } \rho \in \mathbb{S}. \tag{3.22}$$

The weighting functions were chosen as Gaussian functions:

$$\alpha_\ell(\rho) = \frac{\exp\left(-\dfrac{(\rho-\rho_\ell)^2}{2\sigma_\ell^2}\right)}{\displaystyle\sum_{\ell'=1}^{N_\ell} \exp\left(-\dfrac{(\rho-\rho_{\ell'})^2}{2\sigma_{\ell'}^2}\right)}. \tag{3.23}$$

where $\sigma_\ell > 0$ denotes the standard deviation of the Gaussian weighting function associated with the ℓ-th local model. σ determines the rate at which its influence decays away from the operating point ρ_ℓ. Choosing a smaller σ results in more weight on the local model with ρ_ℓ closest to ρ, and the opposite for larger σ. In this work, σ was chosen as

$$\sigma = 0.5\Delta\rho, \tag{3.24}$$

where $\Delta\rho$ denotes the distance between neighboring operating points. An example of this choice of weighing function and σ is shown in Figure 3.4. This choice results in some overlap between adjacent weighting functions while maintaining locality of the individual models. Different weighing functions or values of σ were not investigated.

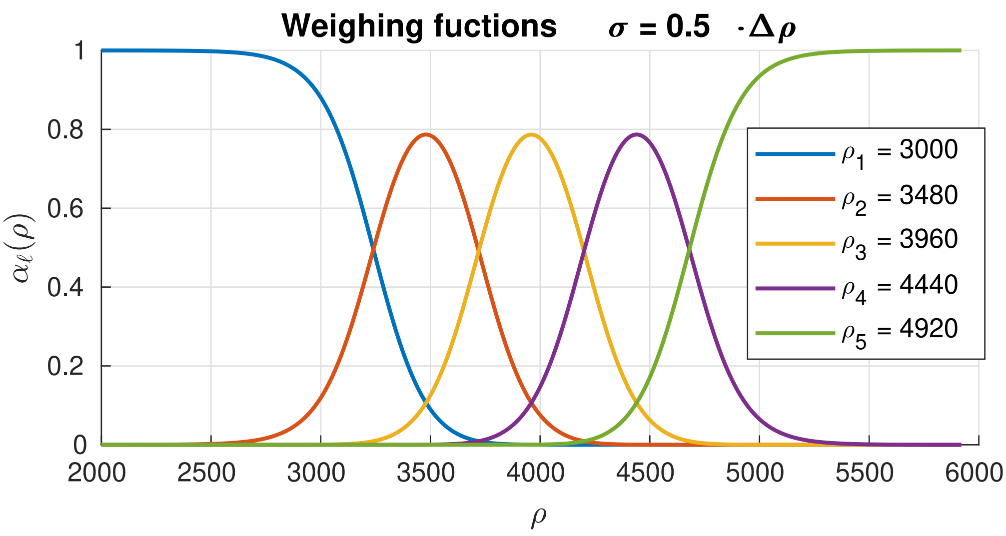

Figure 3.4: Gaussian Weighing functions example, each colored line represents the output weight for a local LTI model at different values of ρ

3.5 Validation Method of Created Models

This section addresses block F in Figure 3.1. To evaluate the performance of different models and approaches, new validation datasets were created. The datasets used for validation differ between experiments. In total, the validation datasets were generated from the following configurations:

- **Constant Rotational Speed:**
  Constant speed measurements of the input shaft. A torque excitation signal is applied as a multisine covering 1–1000 Hz with a frequency resolution of 1 Hz, each frequency has an amplitude of 5 Nmm, and a Schroeder phase distribution.
- **Speed sweep:**
  The rotational speed of the input shaft varies linearly between two defined values, A torque excitation signal is applied as a multisine covering a range of 1–1000 Hz, a resolution of 1 Hz, each frequency has an amplitude of 5 Nmm, and a Schroeder phase distribution.

The estimated models from the different experiments were then supplied with the same input signal as in the validation dataset, and the response from the MBD model and the estimated model was compared. This was done in both frequency domain and the time domain, depending on the metric of interest.

The fit percentage was computed using Normalized Root Mean Squared Error (NRMSE) [24].

$$\text{Fit }\% = 100 \cdot \left(1 - \frac{\|y - \hat{y}\|}{\|y - \text{mean}(y)\|}\right) \tag{3.25}$$

where $\hat{y}$ is the output from the created model and y is the validation data output from the MBD model.

4

Linear Time Invariant Models: Results and Discussion

This chapter presents results from LTI models created with system identification on measured input-output data using the two methods to handle periodic disturbances described in Section 3.3.

4.1 Removing Disturbances

This section presents the results for removing periodic disturbances from block C of the modeling approach shown in Figure 3.1. Models of order 20 were identified using frequency data both containing the full data set (PD-Kept) and with frequencies at periodic disturbances removed (PD-Removed). Frequency data was obtained with frequencies 1–1000 Hz split into 4 experiments with 250 frequencies each using Schroeder phase multisine with amplitude of 50 Nmm for all frequencies. Figure 4.1 shows the frequency response function of data from the MBD model using validation dataset Constant Rotational Speed at 7680 RPM, and Bode plots of the two identified models.

It can be seen that both models are performing similarly at frequencies other than at the two disturbance frequencies. Worth noting is that even though the Bode plot for the PD-Kept model follows the validation data at disturbance frequencies, the peaks are falsely identified as resonance peaks. One result of this is that when the amplitude of the excitation signal changes, the resulting response at the false resonance frequency will also change, but as described in Section 2.3.2, the two peaks from the periodic disturbances do not depend on the excitation signal, meaning that in the real system their amplitude is not affected by excitation signal, as seen in Figure 2.3. Another problem is that the false resonances have poles close to the unit circle, making the PD-Kept model very sensitive to different initial conditions in simulation. A comparison between the two models in time domain is shown in Figure 4.2 where it can be seen that the false resonances in the PD-Kept model cause the model to settle slowly from the incorrect initial states. As expected, it can also be seen that the PD-Removed model shows minimal response at times where the measured response is dominated by the PD.

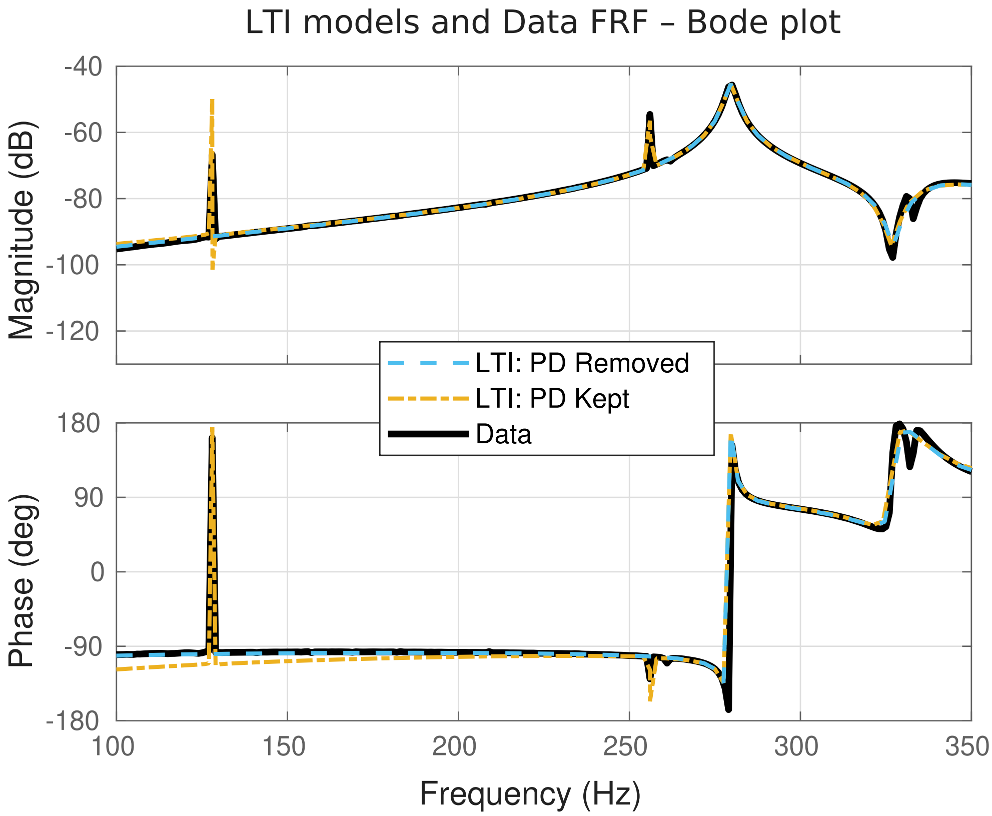

Figure 4.1: Bode plots (100-350 Hz) of the identified models with and without removing periodic disturbances (PD).

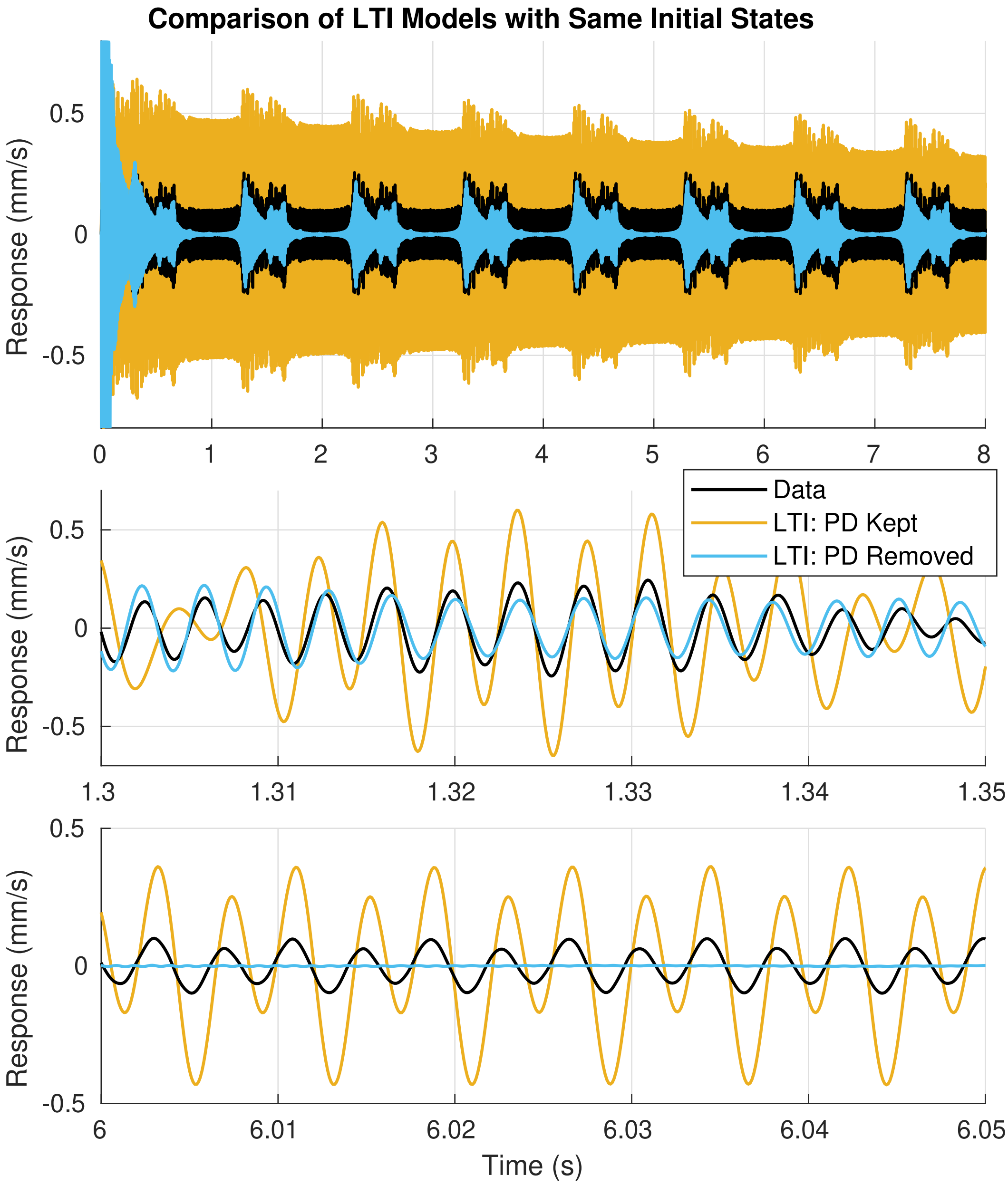

Figure 4.2: Simulated response of two LTI models with PD removed or kept in the estimation data. The top plot shows the full response over 0–8 s. The middle and bottom plots show close-ups of the response around 1.3–1.35 s, where the input–output dynamics dominate, and 6–6.05 s, where the response to the periodic disturbance is dominant

4.2 Adding Disturbances

This section presents the results for adding periodic disturbances from block C of the modeling approach shown in Figure 3.1. The same dataset used in Section 4.1 was used to construct a model including periodic disturbances in the input vector (PD-Added) using the method described in 3.3.2. Figure 4.3 shows a comparison between the frequency response of the MBD model and the PD-Added and PD-Removed LTI models using the Constant Rotational Speed validation set at 7680 RPM.

The difference between the models is that the PD-Added model is also able to reproduce the disturbance peaks correctly. As the response peaks are not modeled as resonances, the change in excitation signal amplitude does not affect the amplitude of the disturbance peaks.

Table 4.1 shows the fit percentage of the magnitude and phase between the frequency response (1-1000 Hz) of the validation data and the PD-Added and PD-Removed models at different rotational speeds using the validation data set Constant Rotational Speed in Section 3.5, excluding the frequency bins of the periodic disturbances.

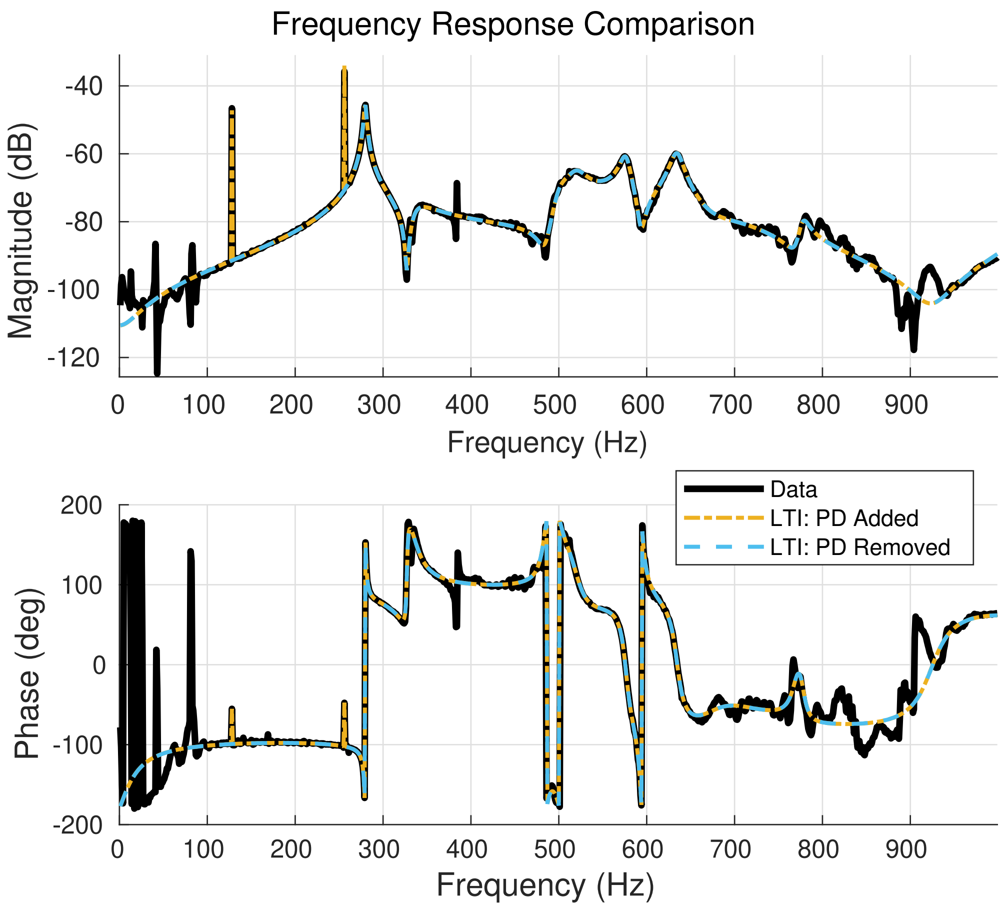

Figure 4.3: Frequency Response of Data from the MBD model and estimated LTI models with periodic disturbances (PD) added and removed.

Table 4.1: LTI Model validation fit percentages excluding frequencies of periodic disturbances, indicating input-output performance.

RPM	$\text{Mag}_{\text{Added}}$ (%)	$\text{Mag}_{\text{Removed}}$ (%)	$\text{Phase}_{\text{Added}}$ (%)	$\text{Phase}_{\text{Removed}}$ (%)
2400	96.338	95.660	76.402	77.810
5280	96.529	96.530	80.886	80.872
7680	96.371	96.371	78.237	78.239

Comparing the PD-Added and PD-Removed models in Figure 4.3 and the percentages for both magnitude and phase of both models in Table 4.1, the results indicate that both models perform similar when simulating the input-output behavior.

Table 4.2 shows the fit percentages of the PD-Added and PD-Removed models but including the frequencies of the periodic disturbances. Figure 4.4 shows the error and the simulated response at each frequency for the PD-removed models. For the PD-Added models the phases of the PDs are unknown, as stated in Section 3.3.2. To get comparable results between models, the phases of the disturbance states were estimated indirectly by estimating the initial state such that the prediction error for the measured output is minimized using MATLAB's `compare()`, the amplitude of the disturbance states were then normalized to 1 as in (3.10).

These results indicate that when the disturbance-state initial conditions are selected to provide the best phase alignment with the measured response, the PD-Added models is able to reproduce the magnitude of the frequency response with a significantly higher fit than the PD-Removed models.

It is worth noting that an increased magnitude error with increasing operating speed is prevalent for the PD-Removed model in Table 4.2. This is likely due to the amplitude of the periodic disturbances increasing at higher RPM, as can be seen in Figure 4.4. This increase in PD amplitude is likely due to the combined effects of the periodic disturbance frequencies becoming more closely aligned with the system's actual resonances at higher operating speeds, and the increased centrifugal forces amplifying the excitation caused by mass imbalance mentioned in Section 2.3.2.

Table 4.2: Model validation fit metrics including periodic disturbance frequencies.

RPM	$\text{Mag}_{\text{Added}}$ (%)	$\text{Mag}_{\text{Removed}}$ (%)	$\text{Phase}_{\text{Added}}$ (%)	$\text{Phase}_{\text{Removed}}$ (%)
2400	96.281	83.036	76.485	77.362
5280	94.565	60.417	80.980	80.781
7680	81.589	21.698	78.293	78.169

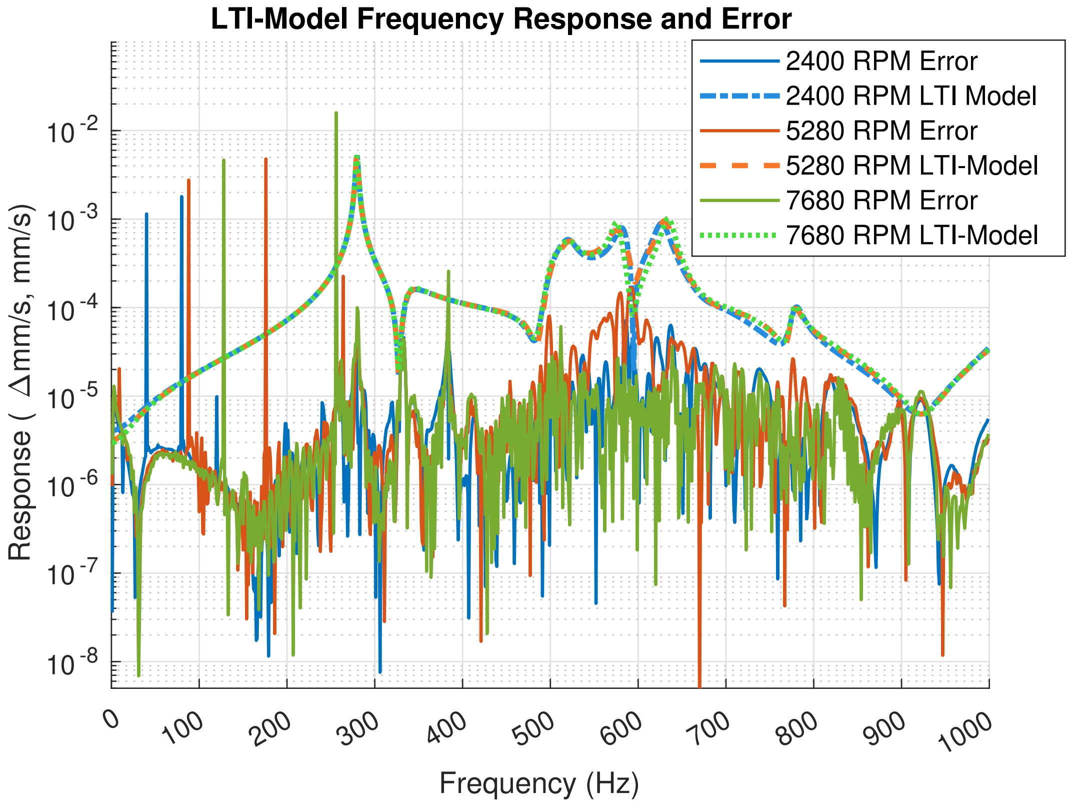

Figure 4.4: Frequency response and magnitude error for three LTI models with PD-Removed at different operating speeds. Dashed lines show the LTI model frequency responses, while solid lines show the corresponding magnitude errors. Error peaks below 400 Hz with an error greater than 10^{-4} mm/s occur at frequencies corresponding to integer multiples of the input shaft rotational frequency, indicating periodic disturbances related to shaft rotation.

4.3 Discussion

Looking at the results from Sections 4.1 and 4.2 it can be seen that removing disturbance frequencies from the data before identifying LTI models reduces the risk of disturbance peaks being falsely identified as resonances. However, by removing the disturbance frequencies from the data, the models are not able to reproduce the peaks that are the true response of the system. Adding disturbance inputs enables the simulation of the true response but also increases the model complexity, and thereby the computational time needed when identifying the model. Adding inputs was also seen to increase the risk of the identification not converging when increasing the model order. If the goal is only to identify a model that reproduces input-output behavior, removing the frequency bins containing the disturbances seems like a valid choice.

5

Modeling Gyroscopic Effects: Results and Discussion

This chapter presents and discusses the results from block E in the method shown in Figure 3.1, modeling the gyroscopic effects of the MBD model using the LPV-modeling methods described in Sections 3.4.1 and 3.4.2. The LPV models were created from LTI models with and without modeling the periodic disturbance.

5.1 LPV With Disturbances Removed

LPV models were created from local LTI models identified with disturbances removed from the data (PD-Removed models) at fixed rotational speeds of the input shaft ranging from 1400 to 8160 RPM, with models estimated at intervals of 480 RPM. The models were created with a model order of 14 states. Both methods to create coherent models described in Section 3.4.1.1 was used and their results are compared in the following subsections.

5.1.1 Initial Guess

Table 5.1 shows the results of simulating LPV models created from LTI models using initial guess to get coherent models compared to the MBD simulation data in the time domain using the validation data set Constant Rotational Speed from Section 3.5. Figure 5.1 shows the Normalized error of the frequency response magnitude for the LPV model constructed by linear interpolation.

Table 5.1: Model fit comparison when using Initial Guess method to get coherent models

RPM	LTI	Lin. Interp. (%)	Basis Quad. (%)	Basis Lin. (%)	Output Interp. (%)
2400	81.570	81.570	81.596	81.564	81.577
5040	–	62.120	62.120	62.087	62.121
5280	59.958	59.958	59.959	59.922	59.959
7680	21.305	21.305	21.305	21.300	21.316
10080	–	39.346	41.476	41.177	39.364

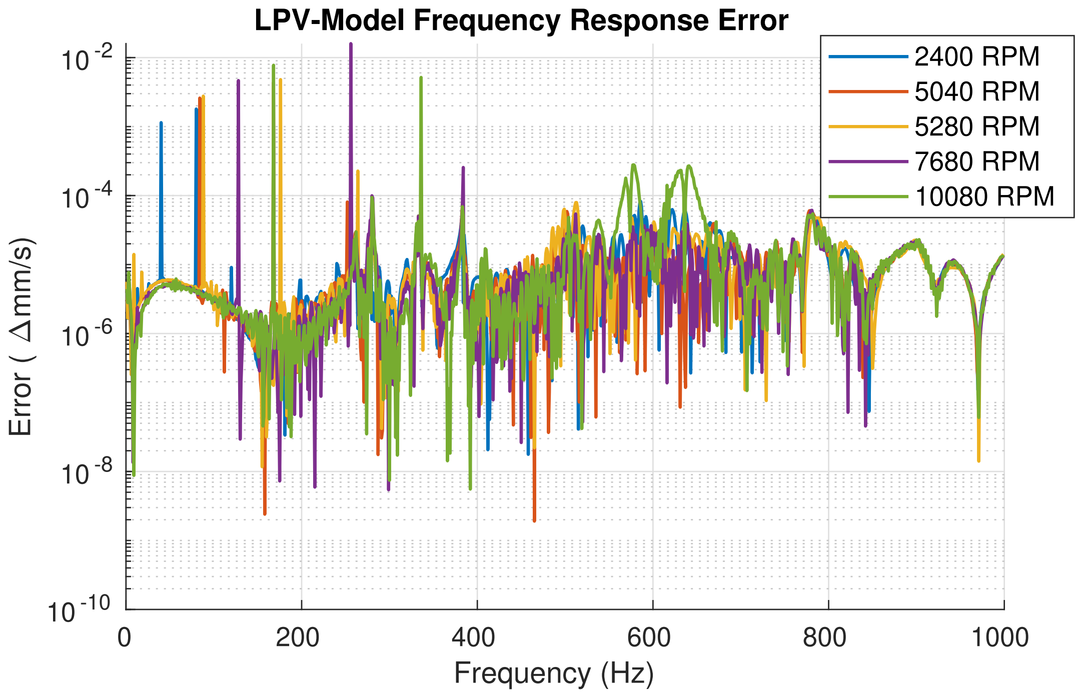

Figure 5.1: Frequency response magnitude error at each frequency for different operating speeds. Peaks with an error greater than 10^{-4} mm/s occur at frequencies corresponding to integer multiples of the input shaft rotational frequency, indicating periodic disturbances related to the shaft rotation.

Comparing the fit percentages of each model in Table 5.1 it can be seen that all proposed methods of creating LPV models yield similar performance for each RPM value at and between estimated local models when local LTI models are created without disturbance. Worth noting is that all models were able to recreate the response at 5040 RPM similarly to an LTI model identified at that RPM, where the LTI model was not used to create LPV models. At 10080 RPM, which is outside the range of used LTI models, both MEP methods were able to match the LTI model while the interpolation methods produced a slightly worse result. As can be seen in Figure 5.1 the largest model errors are at the PD frequencies. At other frequencies, the error is low and similar for all RPMs. Similar to the results for the LTI models in Table 4.2 and Figure 4.4, this suggests that the difference in fit percentage between different operational speeds is closely related to the amplitude of the disturbance frequencies that change depending on rotational speed. Which indicates that the LPV models provide an accurate estimate of the response at other frequencies that are not affected by the PDs.

5.1.2 SMILE Method

Table 5.2 shows the results of simulating LPV models created from LTI models using SMILE method to get coherent models compared to the MBD simulation data in the time domain using the validation data set Constant Rotational Speed from Section 3.5. As the models were created without initial guess, LTI models identified at

Table 5.2: Model fit comparison when using SMILE method to get coherent models

RPM	LTI	Lin. Interp. (%)	Basis Quad. (%)	Basis Lin. (%)	Output Interp. (%)
2400	81.898	81.755	81.728	81.626	81.965
5040	–	62.071	62.074	61.836	62.081
5280	59.912	59.912	59.913	59.690	59.917
7680	21.142	21.142	21.143	21.137	21.198
10080	–	39.080	40.783	40.277	39.17

1920-2880 RPM were discarded when interpolating due to different modes being identified. Output interpolation used all LTI models in the range.

Comparing the model fit percentage at each RPM, the results indicate that all proposed methods of creating LPV models yield similar performance for RPM values at and between estimated local models when identifying coherent LTI models to be used when constructing LPV models. Similarly to the results in Table 5.1, the difference in fit percentage at different RPMs is likely caused by the difference in amplitude of the PDs, as can be seen in Figure 4.4. At other frequencies, the LPV models provide an accurate estimation of the response.

5.1.3 Results with Changing Rotational Speed

Table 5.3 shows the results of simulating the LPV models using the validation data set Speed Sweep from Section 3.5, with operating speed varying linearly with time with 1280 RPM/s, compared to an LTI identified close to the mean RPM within the range. By looking at the fit percentages of all models at each RPM range, it can be observed that all LPV models reproduces the input-output behavior better than using a single LTI model. All methods of element parameterization give similar results for speed ranges inside the range of local LTI models, while linear interpolation performed slightly worse at extrapolation. For time varying rotational speed the LTI models perform worse than all identified LPV models, indicating that modeling the speed dependency improves the model.

Table 5.3: Model fit comparison across time and operating speed ranges for different modeling approaches.

Time range (s)	RPM range	LTI (%) [RPM]	Lin. Interp. (%)	Basis Quad. (%)	Basis Lin. (%)
0.0 – 2.5	1280–4480	74.23 [2880]	74.37	74.34	74.32
2.5 – 5.0	4480–7680	54.92 [6240]	55.81	55.84	55.82
0.0 – 5.0	1280–7680	62.22 [4320]	64.05	64.06	64.03
0.0 – 11.0	1280–14080	23.36 [8160]	24.68	25.60	25.75

5.1.4 Discussion

The results show that all LPV modeling methods produce similar results inside the range the are identified at, that are close to LTI models identified at that RPM. Outside this range, the basis function models performed better than the linear interpolation method. This is expected as the linear interpolation method do not change matrix elements beyond the outermost identified LTI model, and the output interpolation converges to that same model. The interpolation methods are also more sensitive to outliers, while the quadratic basis function model is the only model capable to handle quadratic behavior even with sparse LTI models.

5.2 LPV with Disturbances Added

This section provides the results from creating LPV models from locally estimated LTI models with the periodic disturbances included (PD-Added models). LPV models were created from models of order 8 identified at fixed rotational speeds of the input shaft ranging from 1400 to 8160 RPM, with models estimated at intervals of 480 RPM.

5.2.1 Static Rotational Speeds

The results from validating the LPV models are shown in Table 5.4, data set Constant Rotational Speed from Section 3.5 was used. As mentioned in Section 3.3.2 the phases of disturbances are unknown. For these results the phases of the disturbance states were estimated indirectly by estimating the initial state such that the prediction error for the measured output is minimized using MATLAB's `compare()`, the amplitude of the disturbance states were then normalized to 1 as in equation (3.10). Local models were identified using the initial guess method described in Section 3.4.1.1. Figure 5.2 shows the MEP of one of the elements in $\boldsymbol{G}$. It can be seen that neither of the basis functions are able to follow the variation of the matrix elements accurately.

Table 5.4: Model fit comparison across RPM for different modeling approaches. Negative fit values are reported as $< 0\%$, indicating performance worse than a constant mean-value prediction.

RPM	LTI (%)	Lin. Interp. (%)	Basis Quad. (%)	Basis Lin. (%)
2400	88.191	88.191	43.384	< 0
2640	–	88.528	8.9452	< 0
4080	–	88.917	< 0	< 0
5040	–	89.481	89.124	< 0
5280	88.991	88.991	54.002	< 0
6480	–	89.565	< 0	< 0
7680	81.593	81.593	70.494	< 0
9360	–	< 0	< 0	< 0
10080	–	< 0	< 0	< 0

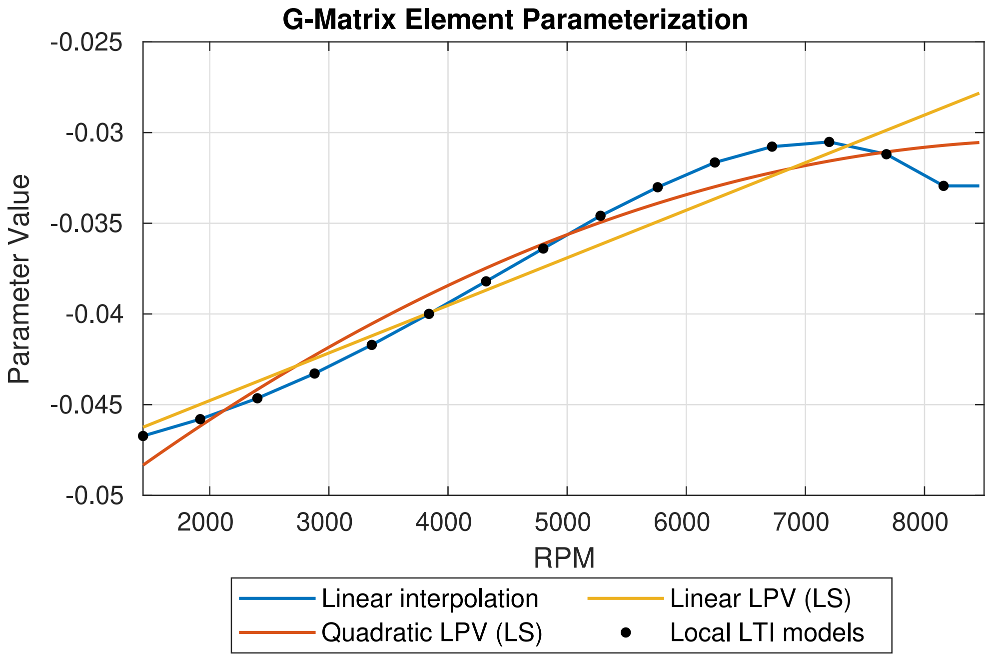

Figure 5.2: Different parameterizations of a single $\boldsymbol{G}$-matrix element obtained from locally identified LTI models.

Looking at the fit percentages and the $\boldsymbol{G}$ element parametrization figure, the LPV model using linear interpolation seems to accurately reproduce the output signal inside of the interpolation range. However, keeping the outermost LTI model for extrapolation does not yield a good fit, indicated by a fit < 0 for rotational speeds 9360 and 10080. The fit percentages for the quadratic and linear basis functions also indicate that incorrect parameterization of the matrix elements results in poor model performance. Using basis functions other than linear or quadratic to parametrize the $\boldsymbol{G}$-matrix elements could possibly result in a more correct parameterization, leading to a better fit and enabling extrapolation.

5.2.2 Changing Rotational Speed

The results from validating the LPV model constructed by linear interpolation with the data set Speed Sweep from Section 3.5 are shown in Table 5.5. The phases of the initial disturbance states were estimated using a least-squares estimate of the initial states, the derivation can be seen in Appendix A, and the amplitude of the disturbance states were then normalized to 1 as in equation (3.10).

The results indicate that the linear interpolated LPV model using PD-Added gives a better fit also with varying RPM. Figures 5.3–5.4 shows the measured response from the Speed Sweep and the estimated response using LPV models PD-Added and PD-Removed. The figures indicate that PD-Added is able to recreate the amplitude of the disturbances. Figure 5.5 shows the response in the time domain over a short amount of time. It can be observed that the disturbance phase is not perfectly aligned with the measured data.

Table 5.5: Model fit comparison across time and operating speed ranges. LPV models are constructed with linear interpolation.

Time range (s)	RPM range	LPV: PD-Removed (%)	LPV: PD-Added (%)
0.0 – 10	1600–4800	66.32	70.99
10 – 20	4800–8000	37.85	40.53
0.0 – 20	1600–8000	47.60	50.67

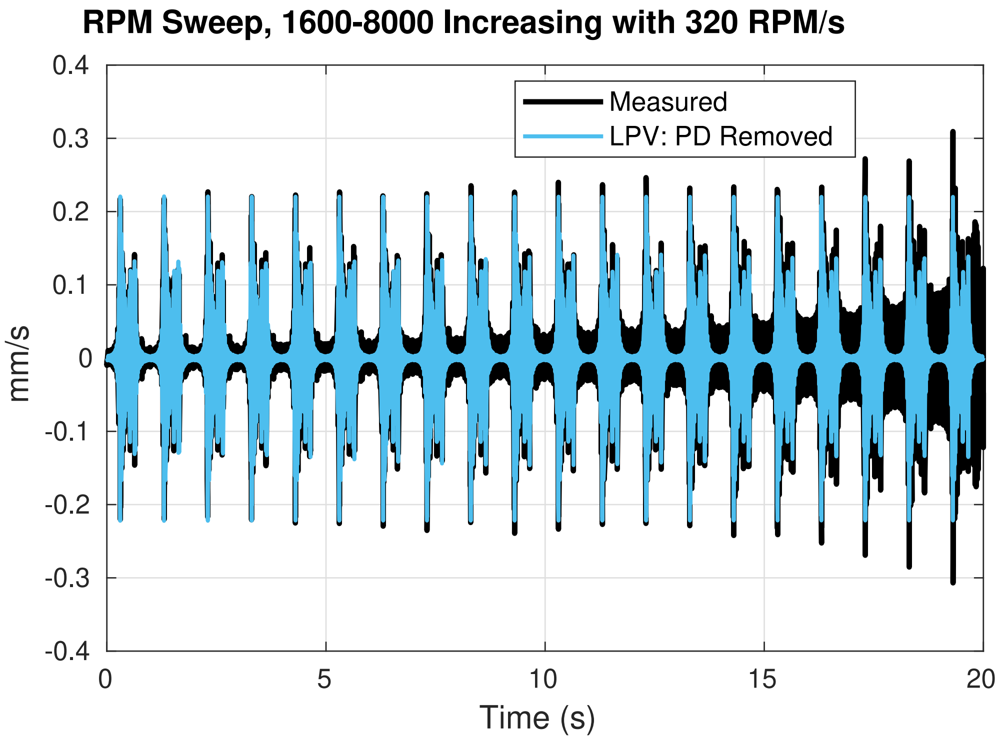

Figure 5.3: Simulated response of LPV model with PD Removed compared to the measured response.

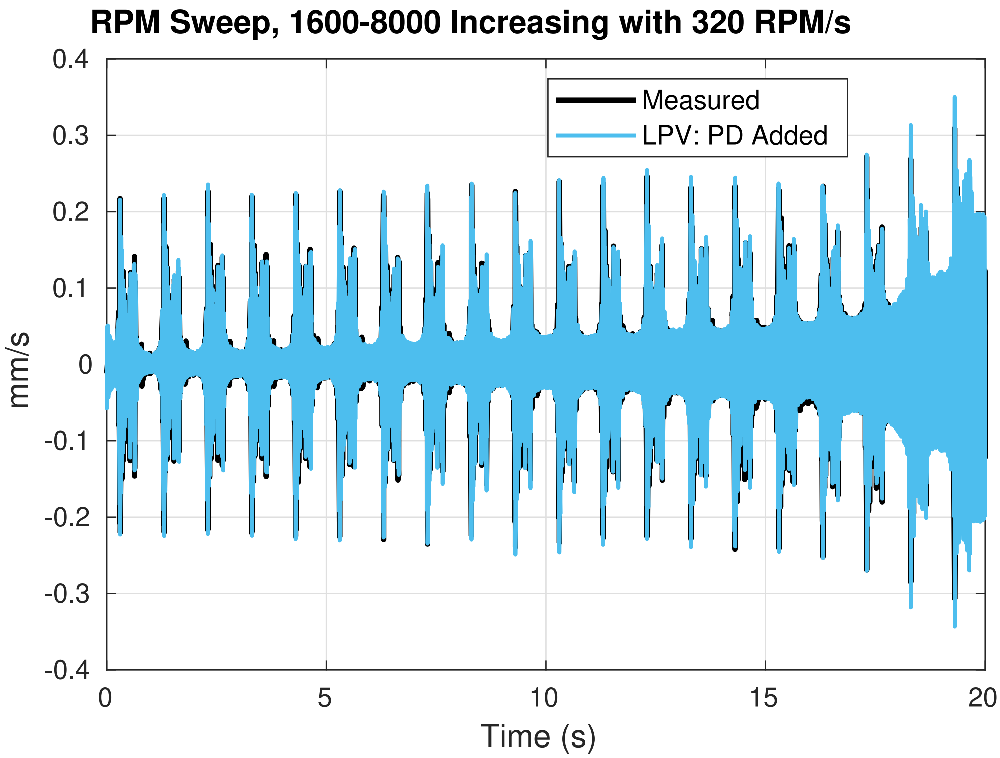

Figure 5.4: Simulated response of LPV model with PD Added compared to the measured response. A zoomed-in view of the time interval from 19.07 to 19.115 s is shown in Figure 5.5.

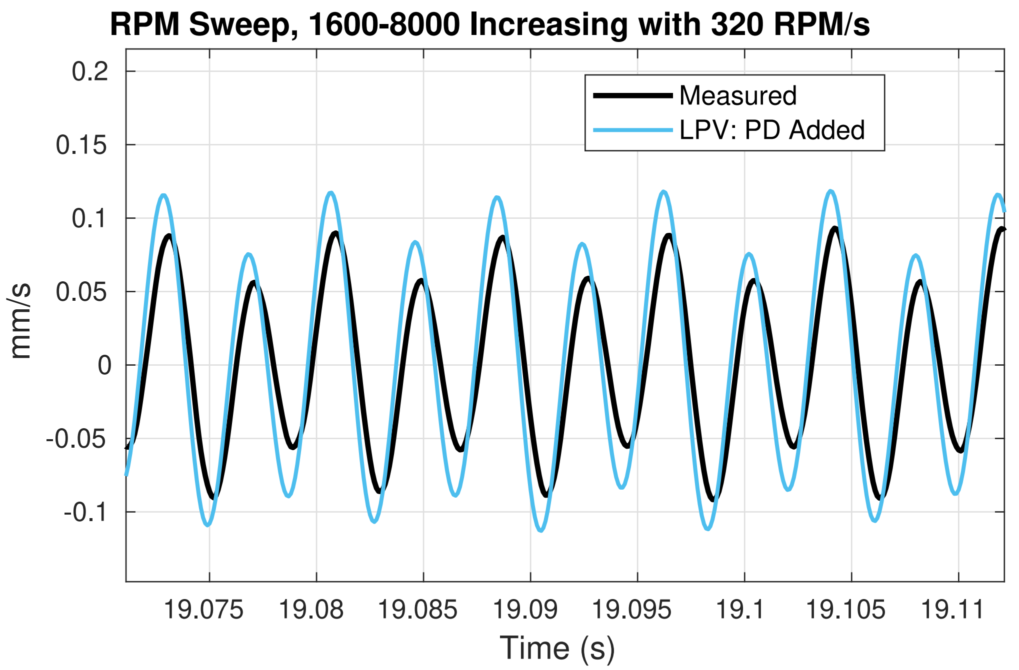

Figure 5.5: Zoomed-in view of the simulated response of the LPV model with PD Added compared to the measured response. The same data are shown over the full time interval in Figure 5.4.

When estimating the phase of the initial disturbance states, different methods of estimation gives slightly different phase results. When comparing the performance of PD-Added to the validation data, the phase of the disturbance states has a significant effect on the fit. Nevertheless, the least-squares-based phase estimation method used for these results indicates that the inclusion of disturbance states is beneficial. While the estimated phases are not exact, incorporating disturbance states leads to a clear improvement in model fit compared to not including them. This also suggests that even better performance could be achieved by improving the angle estimation methods.

6

Conclusions

This chapter covers the key conclusions and recommendations for future work to build on these findings.

6.1 Conclusions About LTI Modeling

The results show that the system identification methods used in this work can produce linear time-invariant models that describe the input-output behavior of the MBD driveline at discrete operating points. The models capture the main dynamic characteristics of the system around the operating points, including its dominant resonant behavior. However, the LTI models do not capture the variation in the system dynamics between operating points or the periodic dynamics caused by asymmetric stiffness, explained in Section 2.3.2. These effects therefore require either separate models at different operating points or an extension of the modeling approach. A key challenge in the identification procedure is the presence of periodic disturbances, illustrated in Figure 2.3. Two methods, presented in Section 3.3, were investigated to reduce the influence of these disturbances on the identified system dynamics.

Both investigated disturbance handling methods are able to construct models without introducing incorrectly identified dynamics such as false resonances. By adding inputs with the same frequency as the periodic disturbance, models can be created that accurately reproduce the disturbances with the correct amplitudes.

These findings indicate that reliable local linear models can be obtained even when periodic effects are present by employing the excitation and modeling strategies presented in this thesis.

6.2 Conclusions About LPV Modeling

The identified local LTI models were successfully used to create parameter varying models that accurately reproduce the system behavior at constant and varying rotational speeds different from the operating points used during the identification step.

The LPV modeling approach is also expected to work for other scheduling variables such as load variations as well. However additional testing is required to confirm these expectations.

Overall, the results show that combining local LTI modeling with the different LPV modeling methods provides a promising framework for creating reduced models of BEV driveline systems.

6.3 Future Work

This section lists some directions in which the methodology used in this work could be further developed and extended.

The current approach does not explicitly model the frequency modulation caused by asymmetric stiffness, described in Section 2.3.2. Instead, this effect was removed by conducting multiple experiments. Future work could investigate an approach that captures both the dependency of the system dynamics on rotational velocity and the periodic dynamics caused by asymmetric stiffness. One possible approach is to formulate the system as a Linear Time Periodic (LTP) system, where the dynamic behavior varies periodically. Subspace methods can be used to identify linear models describing this periodic behavior [25]. These LTP models could then be represented as parameter-varying models using the methods presented in this work.

Early testing also showed that including more output signals improved observability, increasing the possible model order. This might be because some modes show up with high amplitude at some points and very low, but still existing, at other points. Using multiple outputs should reduce the risk of the smaller resonances of being mixed up with noise. The possibility to use multiple load signals could also be investigated.

Another benefit of constructing a multiple output model is that measuring one of the modeled outputs can enable better estimation of another. To accurately estimate the output in real time the phase of the disturbance states need to be known. The goal of projecting the input signals to the $\boldsymbol{A}$ matrix is for the disturbance states to be the same for all outputs. This should enable measuring the disturbance phase at one point, and thereby estimate the disturbance states. If the disturbance states are correctly estimated the disturbance model should correctly estimate the output at all other outputs.

Finally, the methods presented in this work provide models in state-space form without physical interpretability of the states. An interesting continuation would be to investigate the possibility of identifying the system such that the states carry physical meaning, with the goal of obtaining a model similar in structure to Equation 2.2.

Bibliography

[1] L. Ljung, "Estimating Linear Time-invariant Models of Nonlinear Time-varying Systems," *European Journal of Control*, vol. 7, no. 2, pp. 203–219, 2001.

[2] P. V. Overschee and B. D. Moor, "N4sid: Subspace algorithms for the identification of combined deterministic-stochastic systems," *Automatica*, vol. 30, no. 1, pp. 75–93, 1994.

[3] E. Reynders and G. D. Roeck, "Reference-based combined deterministic–stochastic subspace identification for experimental and operational modal analysis," *Mechanical Systems and Signal Processing*, vol. 22, no. 3, pp. 617–637, 2008.

[4] L. MEVEL, L. HERMANS, and H. VAN DER AUWERAER, "APPLICATION OF A SUBSPACE-BASED FAULT DETECTION METHOD TO INDUSTRIAL STRUCTURES," *Mechanical Systems and Signal Processing*, vol. 13, no. 6, pp. 823–838, 1999.

[5] J. Bokor and G. Balas, "Linear parameter varying systems: A geometric theory and applications," *IFAC Proceedings Volumes*, vol. 38, no. 1, pp. 12–22, 2005. 16th IFAC World Congress.

[6] A. K. Al-Jiboory, G. Zhu, S. S.-M. Swei, W. Su, and N. T. Nguyen, "LPV modeling of a flexible wing aircraft using modal alignment and adaptive gridding methods," *Aerospace Science and Technology*, vol. 66, pp. 92–102, 2017.

[7] B. Kulcsár, J. Dong, J.-W. van Wingerden, and M. Verhaegen, "LPV Subspace Identification of a DC motor with unbalanced disc," *IFAC Proceedings Volumes*, vol. 42, no. 10, pp. 856–861, 2009. 15th IFAC Symposium on System Identification.

[8] J. De Caigny, R. Pintelon, J. F. Camino, and J. Swevers, "Interpolated modeling of LPV systems," *IEEE Transactions on Control Systems Technology*, vol. 22, no. 6, pp. 2232–2246, 2014.

[9] Q. Zhang, L. Ljung, and R. Pintelon, "On local LTI model coherence for lpv interpolation," *IEEE Transactions on Automatic Control*, vol. 65, no. 8, pp. 3671–3676, 2020.

[10] A. Bourdon, H. Andre, and D. Rémond, "Introducing angularly periodic disturbances in dynamic models of rotating systems under non-stationary conditions," *Mechanical Systems and Signal Processing*, vol. 44, no. 1-2, pp. 60–71, 2014.

Special Issue on Instantaneous Angular Speed (IAS) Processing and Angular Applications.

[11] J.-W. van Wingerden, A. Hulskamp, T. Barlas, I. Houtzager, H. Bersee, G. van Kuik, and M. Verhaegen, "Two-degree-of-freedom active vibration control of a prototyped "smart" rotor," *IEEE Transactions on Control Systems Technology*, vol. 19, no. 2, pp. 284–296, 2011.

[12] G. Kerschen, K. Worden, A. F. Vakakis, and J.-C. Golinval, "Past, present and future of nonlinear system identification in structural dynamics," *Mechanical Systems and Signal Processing*, vol. 20, no. 3, pp. 505–592, 2006.

[13] M. I. Friswell, J. E. T. Penny, S. D. Garvey, and A. W. Lees, *Fundamentals of Rotor Dynamics*. No. 26 in Cambridge Aerospace Series, Cambridge: Cambridge University Press, 2010.

[14] S. S. Rao, *Mechanical Vibrations*. Upper Saddle River, NJ: Pearson, 5 ed., 2011.

[15] A. Brandt, *Noise and Vibration Analysis: Signal Analysis and Experimental Procedures*. John Wiley & Sons, 2011.

[16] T. Rossing, *Modal Analysis*, pp. 1127–1138. New York, NY: Springer New York, 2007.

[17] T. Söderström and P. Stoica, *System Identification*. Englewood Cliffs, NJ: Prentice Hall, 1989.

[18] T. M. Inc., "System identification toolbox version 9.15 (r2021b)," 2021.

[19] AVL, "AVL Excite M." `https://www.avl.com/en-se/simulation-solutions/software-offering/simulation-tools-a-z/avl-excite-m`, 2026. [Online; accessed 04-Feb-2026].

[20] T. M. Inc., "MATLAB version: 9.11.0 (r2021b)," 2021.

[21] R. Pintelon and J. Schoukens, *System Identification: A Frequency Domain Approach*. IEEE Press, 2001.

[22] Wu, Bin-Yi, Qin, Xian-Sheng, Zhang, Shun-Qi, Bai, Jing, Xue, Ting, and Schmidt, Rüdiger, "Unknown disturbance estimation for vibration systems using distributed piezoelectric sensors," *Mechanics & Industry*, vol. 19, no. 5, p. 506, 2018.

[23] Q. Zhang, "LPV system local model interpolation based on combined model reduction," *IFAC-PapersOnLine*, vol. 51, no. 15, pp. 1104–1109, 2018. 18th IFAC Symposium on System Identification SYSID 2018.

[24] MathWorks, "goodnessOfFit," 2026. MATLAB System Identification Toolbox documentation, accessed 2026-05-10.

[25] Uyanık, U. Saranlı, M. M. Ankaralı, N. J. Cowan, and Morgül, "Frequency-Domain Subspace Identification of Linear Time-Periodic (LTP) Systems," *IEEE Transactions on Automatic Control*, vol. 64, no. 6, pp. 2529–2536, 2019.

A

Least Squares Estimation of Initial States

This chapter presents the derivation of the initial-state estimate for an LPV model with varying rotational speed. The LPV model augmented with disturbance states is described by

$$\boldsymbol{z}_{k+1} = \begin{bmatrix} \boldsymbol{A}(\rho_k) & \boldsymbol{G}(\rho_k) \\ \boldsymbol{0} & \boldsymbol{R}(\rho_k) \end{bmatrix} \boldsymbol{z}_k + \begin{bmatrix} \boldsymbol{B}(\rho_k) \\ \boldsymbol{0} \end{bmatrix} \boldsymbol{u}_k, \tag{A.1a}$$

$$\boldsymbol{y}_k = \begin{bmatrix} \boldsymbol{C}(\rho_k) & \boldsymbol{0} \end{bmatrix} \boldsymbol{z}_k + \boldsymbol{D}(\rho_k)\boldsymbol{u}_k. \tag{A.1b}$$

where

$$\boldsymbol{z}_k = \begin{bmatrix} \boldsymbol{x}_k \\ \boldsymbol{d}_k \end{bmatrix}, \tag{A.2}$$

contains both the physical states and the disturbance states.

The system matrices depend on the measured rotational speed through the scheduling parameter ρ. Evaluating the LPV model at each sampling instant yields the time-varying matrices

$$\boldsymbol{A}_k,\ \boldsymbol{B}_k,\ \boldsymbol{C}_k,\ \boldsymbol{D}_k,\ \boldsymbol{G}_k. \tag{A.3}$$

The disturbance oscillators are described by

$$\boldsymbol{R}_k = \mathrm{blkdiag}(\boldsymbol{R}_{1,k}, \boldsymbol{R}_{2,k}), \tag{A.4}$$

where

$$\boldsymbol{R}_{n,k} = \begin{bmatrix} \cos(\theta_{n,k}) & -\sin(\theta_{n,k}) \\ \sin(\theta_{n,k}) & \cos(\theta_{n,k}) \end{bmatrix}, \tag{A.5}$$

with

$$\theta_{1,k} = \omega_k T_s, \qquad \theta_{2,k} = 2\omega_k T_s, \tag{A.6}$$

and ω_k denoting the rotational speed in rad/s.

Define the augmented matrices

$$A_{\text{aug},k} = \begin{bmatrix} \boldsymbol{A}_k & \boldsymbol{G}_k \\ \boldsymbol{0} & \boldsymbol{R}_k \end{bmatrix}, \qquad \boldsymbol{B}_{\text{aug},k} = \begin{bmatrix} \boldsymbol{B}_k \\ \boldsymbol{0} \end{bmatrix}, \qquad \boldsymbol{C}_{\text{aug},k} = \begin{bmatrix} \boldsymbol{C}_k & \boldsymbol{0} \end{bmatrix}. \tag{A.7}$$

The time-varying state-transition matrix is defined recursively as

$$\boldsymbol{\Phi}_0 = \boldsymbol{I}, \qquad \boldsymbol{\Phi}_{k+1} = \boldsymbol{A}_{\text{aug},k} \boldsymbol{\Phi}_k. \tag{A.8}$$

The state at time instant k can then be expressed as

$$\boldsymbol{z}_k = \boldsymbol{\Phi}_k \boldsymbol{z}_0 + \sum_{i=0}^{k-1} \boldsymbol{\Phi}_{k-i-1} \boldsymbol{B}_{\text{aug},i} \boldsymbol{u}_i. \tag{A.9}$$

Substituting into the output equation (A.1b) gives

$$\boldsymbol{y}_k = \boldsymbol{C}_{\text{aug},k} \boldsymbol{\Phi}_k \boldsymbol{z}_0 + \boldsymbol{y}_{u,k}, \tag{A.10}$$

where $\boldsymbol{y}_{u,k}$ denotes the output generated by the known input sequence with $\boldsymbol{z}_0 = 0$. Stacking the outputs over an estimation horizon of length N,

$$\boldsymbol{Y}_{\text{meas}} = \begin{bmatrix} \boldsymbol{y}_0 \\ \boldsymbol{y}_1 \\ \vdots \\ \boldsymbol{y}_{N-1} \end{bmatrix}, \qquad \boldsymbol{Y}_u = \begin{bmatrix} \boldsymbol{y}_{u,0} \\ \boldsymbol{y}_{u,1} \\ \vdots \\ \boldsymbol{y}_{u,N-1} \end{bmatrix}, \tag{A.11}$$

where $\boldsymbol{y}_k$ denotes the measured output at time instant k, yields

$$\boldsymbol{Y}_{\text{meas}} = \boldsymbol{Y}_u + \boldsymbol{H} \boldsymbol{z}_0 + e, \tag{A.12}$$

with

$$\boldsymbol{H} = \begin{bmatrix} \boldsymbol{C}_{\text{aug},0} \Phi_0 \\ \boldsymbol{C}_{\text{aug},1} \Phi_1 \\ \vdots \\ \boldsymbol{C}_{\text{aug},N-1} \Phi_{N-1} \end{bmatrix}, \tag{A.13}$$

is a finite-horizon observability matrix evaluated along the measured scheduling trajectory, and e is the output prediction error. The initial-state estimate is obtained by minimizing the output prediction error,

$$\hat{\boldsymbol{z}}_0 = \arg\min_{\boldsymbol{z}_0} \left\| \boldsymbol{Y}_{\text{meas}} - \boldsymbol{Y}_u - \boldsymbol{H}\boldsymbol{z}_0 \right\|_2^2 . \tag{A.14}$$

The least-squares solution is

$$\hat{\boldsymbol{z}}_0 = \left(\boldsymbol{H}^T\boldsymbol{H}\right)^{-1} \boldsymbol{H}^T \left(\boldsymbol{Y}_{\text{meas}} - \boldsymbol{Y}_u\right), \tag{A.15}$$

provided that $\boldsymbol{H}$ has full column rank. In practice, the estimate was computed using MATLAB's backslash operator,

$$\hat{\boldsymbol{z}}_0 = \boldsymbol{H} \backslash (\boldsymbol{Y} - \boldsymbol{Y}_u). \tag{A.16}$$

The disturbance phases were extracted from the estimated disturbance states. For a disturbance oscillator represented by

$$\begin{bmatrix} \boldsymbol{a}_n \\ \boldsymbol{b}_n \end{bmatrix}, \tag{A.17}$$

the corresponding phase is

$$\phi_n = \operatorname{atan2}(\boldsymbol{b}_n, \boldsymbol{a}_n). \tag{A.18}$$

DEPARTMENT OF ELECTRICAL ENGINEERING
CHALMERS UNIVERSITY OF TECHNOLOGY
Gothenburg, Sweden
www.chalmers.se

CHALMERS
UNIVERSITY OF TECHNOLOGY